

Entanglement spreading after a geometric quench in quantum spin chains

Vincenzo Alba¹ and Fabian Heidrich-Meisner¹

¹*Department of Physics and Arnold Sommerfeld Center for Theoretical Physics,
Ludwig-Maximilians-Universität München, D-80333 München, Germany*

(Dated: August 27, 2014)

We investigate the entanglement spreading in the anisotropic spin-1/2 Heisenberg (XXZ) chain after a *geometric quench*. This corresponds to a sudden change of the geometry of the chain or, in the equivalent language of interacting fermions confined in a box trap, to a sudden increase of the trap size. The entanglement dynamics after the quench is associated with the ballistic propagation of a magnetization wavefront. At the free fermion point (XX chain), the von Neumann entropy S_A exhibits several intriguing dynamical regimes. Specifically, at short times a logarithmic increase is observed, similar to local quenches. This is accurately described by an analytic formula that we derive from heuristic arguments. At intermediate times partial revivals of the short-time dynamics are superposed with a power-law increase $S_A \sim t^\alpha$, with $\alpha < 1$. Finally, at very long times a steady state develops with constant entanglement entropy, apart from oscillations. As expected, since the model is integrable, we find that the steady state is *non* thermal, although it exhibits *extensive* entanglement entropy. We also investigate the entanglement dynamics after the quench from a finite to the infinite chain (sudden expansion). While at long times the entanglement vanishes, we demonstrate that its relaxation dynamics exhibits a number of scaling properties. Finally, we discuss the short-time entanglement dynamics in the XXZ chain in the gapless phase. The same formula that describes the time dependence for the XX chain remains valid in the whole gapless phase.

I. INTRODUCTION

The recent extraordinary progress achieved with trapped cold-atomic gases experiments has boosted a renewed theoretical interest in the dynamics of isolated quantum many-body systems out-of-equilibrium [1–3]. Highly-investigated topics include the relaxation dynamics [4–9], thermalization [5, 10] in out-of-equilibrium steady states, and transport properties [11–13]. A popular out-of-equilibrium experiment is the so-called *quantum quench*, in which a system is initially prepared in the ground state of a many-body quantum Hamiltonian, and a non-trivial unitary dynamics is then induced by changing instantaneously (i.e., “quenching”) one (or many) control parameters. Depending on whether this change happens locally or in the whole system, the quench falls into the class of local or global quenches, respectively.

Entanglement measures are nowadays accepted as useful tools to extract universal properties of quantum many-body systems, both in and out-of-equilibrium [14–20]. Considering a bipartition of a system that is in a pure state $|\psi\rangle$ into parts A and B , a standard measure of their mutual entanglement is the von Neumann entropy S_A

$$S_A = -\text{Tr} \rho_A \log \rho_A. \quad (1)$$

Here ρ_A is the reduced density matrix for A , obtained after tracing part B from the full density matrix $\rho \equiv |\psi\rangle\langle\psi|$.

The real-time entanglement dynamics (and that of related quantities) after a quantum quench has been intensively investigated in recent years, both analytically (using conformal field theory [21–23] and for exactly solvable models [24–36]) and numerically [37–46]. The nature of the quench is strikingly reflected in the time dependence of the von Neumann entropy: while local quenches are associated with a logarithmic growth [21, 23, 24], a more dramatic (linear) behavior is observed in global quenches [22, 37, 38, 47]. This is related to the different excess energy density, measured with respect to

the ground-state energy of the post-quench Hamiltonian. This excess energy remains finite in the global quench protocol, whereas it vanishes in the local one, upon increasing the system size. We mention that a scheme for measuring entanglement dynamics in cold-atomic gases experiments has recently been proposed in Ref. 48, 49.

In our work we focus on a situation that is intermediate between a local and a global quench, considering the real-time entanglement dynamics following an instantaneous change of the geometry or the size of the system, the so-called *geometric quench*, as discussed in Ref. 50. To be specific, we study the spin-1/2 XXZ chain in the gapless phase. The quench protocol is described as follows (cf. Fig. 1): initially two chains A and B are prepared in the ground state of the XXZ model in the sector with zero and maximum magnetization (i.e., fully polarized), respectively. The unitary dynamics under the XXZ Hamiltonian is then induced by connecting the two chains. Alternatively, after mapping the XXZ chain onto a system of interacting fermions confined in a box trap (i.e., chain A), the geometric quench is equivalent to suddenly increasing the trap size. Notice that this is similar to the so-called sudden expansion protocol used in cold-atomic gases experiments [11–13, 51], in which particles are released from the trap and expand in an empty lattice. This sudden expansion has been studied theoretically in, e.g., Refs. 44, 52–61.

Clearly, as the two chains are prepared in their respective ground states, the post-quench dynamics is induced by a “defect” at the interface between A and B , which is a distinctive feature of local quenches. On the other hand, the excess energy density is *finite*, as in global quenches. Notice that the initial state after the quench is of the “domain wall” type (i.e., spatially inhomogeneous), and the ensuing out-of-equilibrium dynamics has been at the focus of many recent theoretical studies [33, 34, 62–73]. For instance, the state $|m_A\rangle \otimes |m_B\rangle$, with m_A and m_B being the total magnetization in chain A and B , respectively, provides a ba-

sic setup for studying transport-related questions and non-equilibrium steady-state properties such as the conditions for ballistic or diffusive dynamics in integrable many-body systems in one dimension [74, 75]). In particular, the sub-class of initial states with $m_A = -m_B \equiv m$ has been extensively studied [33, 34, 62, 64–66, 68, 69, 72, 73]. The initial state in our work corresponds to choosing $m_A = 0$ and $m_B = L_B/2$. Interestingly, in the situation with $m_A = -m_B$ it has been found that the magnetization dynamics during the domain wall melting is ballistic close to the free fermion point, super-diffusive at the isotropic point, and diffusive in the gapped phases [64]. While entanglement dynamics from domain wall initial states is interesting as such, it is also important for the simulability of quench dynamics using matrix-product states based methods, such as DMRG (Density Matrix Renormalization Group) [76–78]. For a discussion of transport and local quenches in spin chains in non-equilibrium for other initial conditions, see Ref. [79–86]. We should also mention that transport and entanglement properties have also been studied in the dynamics induced by local impurities [27, 30, 39, 41, 87].

Summary of the results.— In this work we fully characterize the entanglement spreading after a generic geometric quench, focusing on the entanglement entropy between A and B . The spreading of information (and the related entanglement increase) is associated with the propagation of an extended magnetization wavefront. The two edges of the front expand *ballistically* in the A and B parts of the chain, with two different velocities. These coincide at the free-fermion point (XX chain, i.e., vanishing anisotropy), where the wavefront propagates symmetrically. For the XX chain the full magnetization profile, at any time after the quench, is obtained analytically, using a semiclassical reasoning and free-fermionic techniques (as in [88]). For the XXZ chain, although we do not derive analytically the full magnetization profile, we provide an approximate expression describing the central region of the wavefront.

The entanglement evolution exhibits several dynamical behaviors at different time scales. For the XX chain all these dynamical regimes are thoroughly investigated, exploiting the mapping to free fermions. At *short* times, the von Neumann entropy increases logarithmically, as in a local quench. Although the well-known conformal field theory (CFT) result for the local quench [21, 23] does not apply, we provide a heuristic extension of this result to our case, which accurately reproduces the entanglement dynamics. One remarkable consequence is that the entanglement dynamics, apart from a size-dependent shift, is described by a scaling function $f_s(y)$, with $y \equiv t/L_A$ (t is the time after the quench and L_A the size of part A). We numerically demonstrate that the same scaling holds true in the interacting case.

At *intermediate* times the entanglement entropy exhibits revivals of the short-time dynamics, superposed with a power-law increase as $S_A \sim t^\alpha$ (apart from possible multiplicative logarithmic corrections). We numerically extract the exponent α , finding $\alpha < 1$. This suggests that the geometric quench cannot be thought of as a simple superposition of a logarithmic (i.e., local-quench like) and a linear (as in global

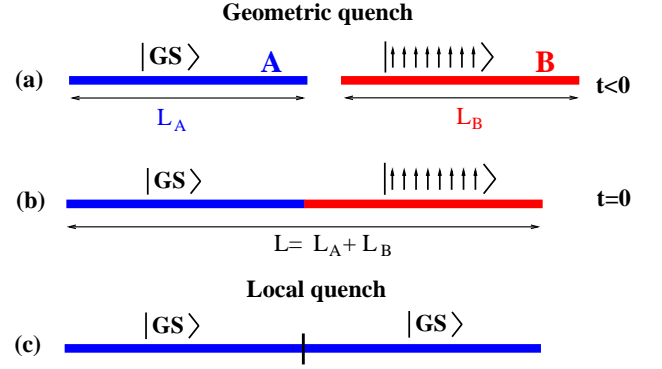


FIG. 1: (a), (b) Geometric quench in XXZ spin chain: quench setup for open boundary conditions. (a) $t < 0$: Two independent chains (A and B) of length L_A and $L_B \equiv L - L_A$ are prepared in the ground state of the XXZ chain in the sectors with zero and maximal magnetization, respectively. (b) $t = 0$: A and B are glued together. Here we consider geometric quenches with several aspect ratios $\omega \equiv L_A/L$, i.e., $0 \leq \omega \leq 1$, focusing on the entanglement between A and B . (c) Example of *typical local* quench protocol: the initial state at $t = 0$ is obtained connecting two *identical* chains prepared in the ground state at zero magnetization.

quenches) behaviors.

At *long* times the system reaches an out-of-equilibrium steady state, and the entropy oscillates around a stationary value. The steady state is *non* thermal and shows features of the initial Fermi surface in part A of the chain. Finally, in spite of the non-thermal nature of the steady state, we demonstrate that the entanglement entropy is *extensive*, and its stationary value can be determined analytically. Similar results have been found in Ref. 33 for the quench from the state $|-m\rangle \otimes |m\rangle$, while the constraints put on steady states due to integrability for a similar set-up and hard-core bosons, which map on the XX model, were discussed in a seminal paper by Rigol et al. [89].

We also discuss the information spreading after the quench from a finite to the infinite chain. In the framework of trapped interacting fermions, this corresponds to removing the trap completely, i.e., to the so-called sudden expansion. While the entanglement entropy vanishes asymptotically (i.e., at large times), its relaxation dynamics shows unexpected scaling behaviors. In particular, the entanglement dynamics is described by a scaling function $f_\ell(z)$ with $z \equiv t/L_A^2$. Furthermore, $f_\ell(z)$ exhibits an intriguing structure: while at $z \ll 1$ one has $f_\ell(z) \sim -\log(1/z)$, a crossover to the behavior $1/z(1 - \log(1/z))$ occurs at $z \sim 1$. Similar scaling behaviors have been observed in the entanglement dynamics of non-interacting fermions in continuous space released from a trap [90–92].

Finally, by means of tDMRG [93, 94] (time-dependent Density Matrix Renormalization Group) simulations, we investigate the role of interactions on the short-time entanglement dynamics, focusing on the XXZ spin chain. Our main result is that the same formula used for the XX chain remains valid. Interestingly, since the excitations forming the wavefront propagate in the two parts of the chain with different

velocities, we find that the entanglement spreading rate is not a trivial function of the spinon velocity.

Outline.— This paper is organized as follows. In Sec. II we introduce the XXZ spin chain and the geometric quench protocol. Sections III, IV, V, VI, and VII are devoted to the XX chain. In Sec. III we investigate the magnetization wavefront expansion. An overview of the entanglement dynamics after the quench is given in Sec. IV, while the short-time behavior is discussed in detail in Sec. V. In Sec. VI we characterize the entanglement properties in the steady state. The infinite-chain quench is then discussed in Sec. VII. Finally, in Sec. VIII we investigate the short-time entanglement dynamics in the XXZ model, while a summary is provided in Sec. IX.

II. MODEL & QUENCH PROTOCOL

A. The spin-1/2 XXZ spin chain

The open XXZ spin chain of length L is defined by the Hamiltonian

$$\mathcal{H} = \frac{J}{2} \sum_{i=1}^{L-1} (S_i^+ S_{i+1}^- + h.c.) + J\Delta \sum_{i=1}^{L-1} S_i^z S_{i+1}^z. \quad (2)$$

Here $S_i^\pm \equiv S_i^x \pm iS_i^y$, $S_i^z \equiv S_i^z$ are spin-1/2 operators acting at site i of the chain, and Δ the so-called anisotropy (we set $J = 1$ in Eq. (2)). For a periodic chain an extra term in Eq. (2) connects sites 1 and L . The ground-state phase diagram of the XXZ chain exhibits a gapless spin-liquid phase at $-1 < \Delta \leq 1$, while it is gapped at $|\Delta| > 1$. At $\Delta = 0$ (XX chain) the XXZ chain reduces to a free-fermionic model (cf. Appendix A for more details) [95].

The low-energy spectrum of Eq. (2) is linear in the spin liquid phase, and it is described (along with other low-energy properties) by a conformal field theory (CFT) with central charge $c = 1$. At sufficiently large L one has [96, 97]

$$E_\alpha = LE_{\text{bulk}} + E_{\text{bound}} + \frac{\pi v_s}{L} \left(h_\alpha - \frac{c}{24} \right) + \mathcal{O}(L^{-2}), \quad (3)$$

with E_α being the energy of a low-lying excitation (labeled by $\alpha \in \mathbb{N}$) of Eq. (2). In Eq. (3), E_{bulk} and E_{bound} are the usual bulk (extensive) and a boundary (in presence of non-periodic boundary conditions) contributions, c is the central charge (here $c = 1$), and v_s the spinon velocity. Finally, h_α are the scaling dimensions of the operators (both *primary* operators and their *descendants* [98, 99]) appearing in the CFT. In particular, $\alpha = 0$ (with $h_\alpha = 0$) corresponds to the ground-state energy E_0 . Finite-size deviations from the linear dispersion are accounted for by the $\mathcal{O}(1/L^2)$ term. Notice that Eq. (3) can be thought of as the spectrum of an effective Hamiltonian \mathcal{H}_{CFT} . The two energy scales set by the terms $\sim 1/L$ and $\sim 1/L^2$ in Eq. (3) imply the existence of two typical time scales $t_s^* \sim L/v_s$ (short times) and $t_\ell^* \sim L^2/v_s$ (long times) (here all lengths are measured in units of the lattice constant $a = 1$). We anticipate that the existence of t_s^* and t_ℓ^* will be strikingly reflected in the entanglement dynamics after the quench.

B. Quench protocol and observables

The geometric quench protocol for the XXZ spin chain with open boundary conditions (the generalization to periodic boundary conditions is straightforward) is depicted in Fig. 1. At time $t < 0$ (Fig. 1 (a)) two disconnected chains A and B (of respective lengths L_A and L_B) are prepared in the ground state $|GS\rangle$ of Eq. (2) and in the fully polarized (ferromagnetic) state $|F\rangle \equiv |\uparrow\uparrow \dots \uparrow\rangle$, respectively. The latter is an eigenstate of Eq. (2) at any Δ , with eigenenergy $E \equiv \langle \mathcal{H} \rangle = (L-1)\Delta/4$. At $\Delta \gg -1$ in the gapless phase, which is the region of interest here, $|F\rangle$ is in the high-energy part of the spectrum of Eq. (2), and at the isotropic point ($\Delta = 1$) it is the highest-energy eigenstate.

At $t = 0$ the two chains A and B are connected to form a new one of total length $L \equiv L_A + L_B$ (cf. Fig. 1 (b)). The initial quantum state $|\Psi_{\text{init}}\rangle$ after the quench exhibits a step-like (or “domain wall”) magnetization profile (with $\langle S_i^z \rangle = 0$ and $\langle S_i^z \rangle = 1/2$ for $i \in A$ and $i \in B$ respectively). It is useful to introduce the aspect ratio $0 \leq \omega \leq 1$ as

$$\omega \equiv \frac{L_A}{L}. \quad (4)$$

Finally, at $t > 0$ the chain evolves unitarily under Eq. (2) since $|\Psi_{\text{init}}\rangle$ is not an eigenstate. In this work we focus on the real-time dynamics of the von Neumann entropy S_A between A and B .

C. Geometric vs local quench

It is interesting to compare the geometric quench with a *local* quench [21, 23, 24, 27, 29, 64, 100, 101]. A typical local quench is illustrated in Fig. 1 (c): the initial state $|\Psi_{\text{init}}\rangle$ at $t = 0$ is now obtained by “gluing” together two *identical* copies of the ground state as $|\Psi_{\text{init}}\rangle \equiv |GS\rangle \otimes |GS\rangle$ (which implies that $\omega = 1/2$).

Clearly, the excess energy density, which is defined as $\delta_e \equiv |\langle \Psi_{\text{init}} | \mathcal{H} | \Psi_{\text{init}} \rangle - E_0|/L$, vanishes in the local quench ($\delta_e \sim \mathcal{O}(1/L)$, cf. Eq. (3)) in the limit $L \rightarrow \infty$. Oppositely, in the geometric quench, due to the typically large energy of chain B , one has $\delta_e \sim \mathcal{O}(1)$. As a consequence, while only few low-lying excitations (cf. Eq. (2)) play a role in the dynamics after a local quench, this is certainly different in the geometric quench.

In the CFT framework the initial quantum state $|\Psi_{\text{init}}\rangle$ can be decomposed (in analogy with the standard decomposition in the eigenbasis of Eq. (2)) as

$$|\Psi_{\text{init}}\rangle = \sum_a c_a |\phi_a\rangle \quad (5)$$

where the sum runs over both primary and descendants fields ϕ_a of the CFT. In principle Eq. (5) provides all the necessary information about the post-quench dynamics, after time evolving each eigenstate $|\phi_a\rangle$ of \mathcal{H}_{CFT} with $e^{-i\mathcal{H}_{CFT}t}$.

However, the coefficients c_a in Eq. (5) are not easy to calculate for a generic initial state. For the local quench this is pos-

sible because only one operator (the identity) and its descendants enter in the expansion Eq. (5) [23]. This is related to the fact that $|\Psi_{\text{init}}\rangle$ has substantial overlap only with the ground state of Eq. (2). A prominent consequence is that the entanglement entropy dynamics after a local quench shows perfect revivals (apart from scaling corrections) for $t \sim nt_s^*$, $n \in \mathbb{N}$, at least up to the time $t \sim t_\ell^*$, at which the CFT description is no longer valid, cf. Eq. (3) [23]. Conversely, this will be strikingly different for the geometric quench (cf. Sec. IV).

D. Entanglement dynamics after a local quench

Here we briefly review the CFT result for the entanglement dynamics after the local quench in Fig. 1 (c) [21, 23]. The real-time dynamics of the von Neumann entropy depends only on the central charge c , the boundary conditions, and the spinon velocity v_s . The result reads [23, 27]

$$S_A(t) = \nu \frac{c}{3} \log \left| \frac{L_A}{\pi} \sin \frac{\nu \pi v_s t}{2L_A} \right| + k_\nu. \quad (6)$$

Here $\nu = 1, 2$ are for open (obc) and periodic boundary conditions (pbc), respectively, and k_ν is a non-universal constant. The analog of Eq. (6) for aspect ratios $\omega \neq 1/2$ is also known [23]. It is useful to rewrite Eq. (6) as

$$S_A(t) = \nu \frac{c}{3} \log |\sin(\pi y)| + \nu \frac{c}{3} \log \left(\frac{L_A}{\pi} \right) + k_\nu. \quad (7)$$

Here y is the rescaled time $y \equiv \nu \pi v_s t / (2L_A)$. In Eq. (7) it is apparent that the entropy dynamics is described by a scaling function of y , apart from the shift $\nu c/3 \log(L_A)$. Interestingly, the latter resembles the *equilibrium* ground-state entropy for a block of size L_A embedded in an infinite chain [14–17]. A similar scaling will hold for the entanglement dynamics at short times after the geometric quench (cf. Sec. V). In the limit $t/L_A \ll 1$ (short times), Eq. (6) reduces to [21]

$$S_A(t) = \nu \frac{c}{3} \log t + k_\nu. \quad (8)$$

A similar logarithmic behavior (as in Eq. (6) and Eq. (8)) has been observed in the entanglement dynamics induced by local impurities or perturbations in spin or particle densities [27, 30, 41, 80].

III. MAGNETIZATION WAVEFRONT AFTER THE QUENCH

In this section we discuss the real-time dynamics of the magnetization profile $\langle S_i^z \rangle$ after a geometric quench. Here $\langle \cdot \rangle$ denotes the expectation value with respect to the post-quench wavefunction. We focus on the open XX chain ($\Delta = 0$ in Eq. (2)). At any i, t , $\langle S_i^z \rangle$ can be computed analytically exploiting the mapping to free fermions (see Appendix A).

Figure 2 shows $\langle S_i^z \rangle$ versus $1 \leq i \leq L$ at several times (denoted by different symbols in the figure) after the geometric quench with $\omega \equiv L_A/L = 1/3$ and fixed $L_A = 60$. At $t = 0$,

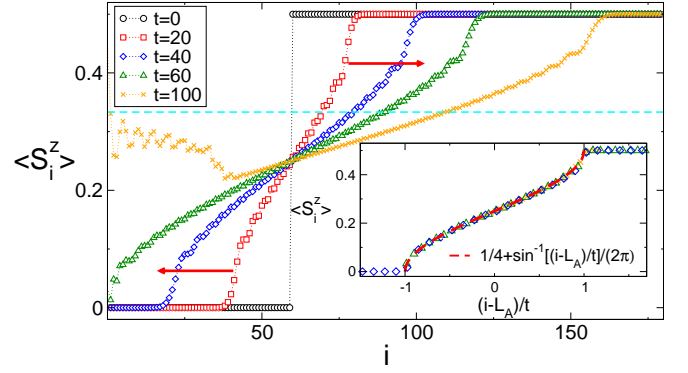


FIG. 2: Magnetization wavefront after the geometric quench with aspect ratio $\omega \equiv L_A/L = 1/3$ (cf. Fig. 1) in the open XX chain: local magnetization $\langle S_i^z \rangle$ at site $0 \leq i < 3L_A$ in the chain. Data are exact results for $L_A = 60$ and several times. At $t = 0$ a step-like profile is present. At $t > 0$ a wavefront forms propagating symmetrically (with $v_s = 1$) in parts A and B (see horizontal arrows). The dashed line is the flat profile expected on average at $t \rightarrow \infty$. At $t = L_A/v_s$ the wavefront is reflected at the (left) boundary of the chain. Inset: rescaled dynamics, $\langle S_i^z \rangle$ versus $(i-L_A)/t$. All data for different times collapse on the same scaling function (dashed line).

a domain-wall profile is present. A magnetization wavefront develops at $t > 0$ (as the domain wall “melts”) with its left and right edges propagating *ballistically* with the same velocity $v = v_s = 1$, with v_s being the spinon velocity, in part A of the chain. At $t = L_A/v_s$, a perfect reflection of the left wavefront edge occurs at the left boundary of the chain. Finally, at large times translational invariance is restored, and a stationary behavior sets in with uniform magnetization (dashed horizontal line in the figure).

The ballistic nature of the wavefront dynamics is further supported by the data shown in the inset of Fig. 2, where we plot $\langle S_i^z \rangle$ versus the rescaled variable $(i-L_A)/t$. Remarkably, all data at different times and positions collapse on the same scaling curve. This curve can be obtained analytically using a semiclassical reasoning that was also applied in Refs. [33, 34, 62, 64, 88, 102] for the quench with initial state $| -m \rangle \otimes | m \rangle$. The result reads

$$\langle S_i^z(t) \rangle = \frac{1}{4} + \frac{1}{2\pi} \sin^{-1} \left[\frac{i-L_A}{v_s t} \right], \quad (9)$$

and is included in Fig. 2 as dashed line. Interestingly, the central region of the profile, at $|(i-L_A)/(v_s t)| \ll 1$, shows a linear dependence on $(i-L_A)/t$:

$$\langle S_i^z(t) \rangle \approx \frac{1}{4} + \frac{i-L_A}{v_s t}. \quad (10)$$

It is natural to expect that Eq. (10) remains valid in the interacting case (i.e., nonzero anisotropy), after taking into account the renormalization, due to interactions, of the spinon velocity v_s (see Sec. VIII A for a numerical check of Eq. (10) in the XXZ spin chain).

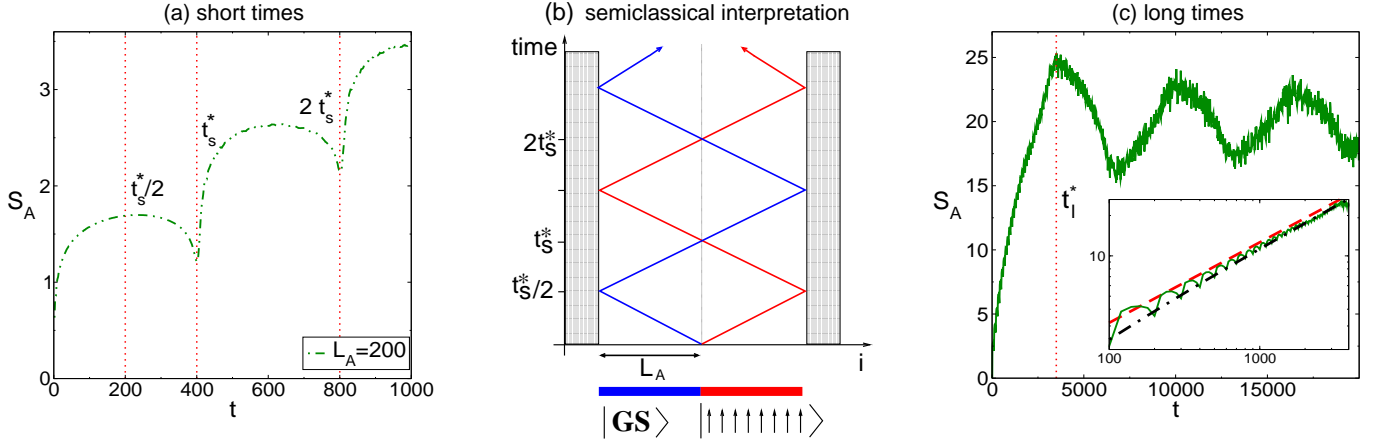


FIG. 3: Entanglement spreading after the geometric quench with aspect ratio $\omega \equiv L_A/L = 1/2$ (cf. Fig. 1) in the open XX chain. (a) von Neumann entropy (dashed-dotted line) S_A for part A of the chain as a function of time: exact results for $L_A = 200$, $0 \leq t \leq t_s^*$ (short times), with $t_s^* \equiv 2L_A/v_s$ where $v_s = 1$ is the spinon velocity. Dotted vertical lines mark the times $t = t_s^*/2, t_s^*, 2t_s^*$. (b) Semiclassical interpretation: entanglement growth is understood in terms of the ballistic propagation (with velocity $v_s = 1$) of free effective excitations (the lines denote their trajectories). These are created at $t = 0$ at the interface between A and B . At $t = t_s^*/2$, perfect reflection at the boundary of the chain occurs. Entanglement “jumps” at $t = mt_s^*, m = 1, 2, \dots$ correspond to excitations crossing the center of the chain. (c) Long-time behavior: at $t \sim t_\ell^* \equiv L_A^2/v_s$ (i.e., after $\mathcal{O}(L_A)$ crossings) the system reaches a steady state with constant entropy (apart from superimposed oscillations). Inset: approach to the steady-state entanglement (data for the same parameters as in the main figure and $0 \leq t \leq t_\ell^*$). A logarithmic scale is used on both axes. The dashed line is $S_A \sim t^\alpha$, with $\alpha \approx 0.6$, whereas the dashed-dotted one is $S_A \sim t^{1/2} \log(t)$.

IV. ENTANGLEMENT SPREADING IN FREE SYSTEMS: OVERVIEW

We now turn to the real-time dynamics of the entanglement entropy S_A between the two parts A and B of the chain. Here we consider the open XX chain, restricting ourselves to an aspect ratio of $\omega = 1/2$ (see Fig. 1). The calculation of the entanglement entropy after the geometric quench in the XX chain is outlined in Appendix C.

Clearly, at $t = 0$, A is in a pure state, implying $S_A = 0$. Exact numerical data at $t > 0$ after the quench (with fixed $L_A = 200$) are shown in Fig. 3 [dashed-dotted line in panels (a) and (c)]. S_A exhibits different behaviors at different time scales. At short times $t \leq t_s^*/2$, with $t_s^* \equiv 2L_A/v_s$, (cf. Fig. 3 (a)) the entanglement entropy grows logarithmically as in a local quench. In the time-interval $t_s^*/2 \lesssim t \leq t_s^*$, it slightly decreases reflecting the finite size of part A .

At intermediate times $t_s^* < t \leq t_\ell^*$ (cf. Fig. 3 (c)), S_A grows with a power law (cf. the inset in Fig. 3 (c)). A fit to $S_A \sim t^\alpha$ yields $\alpha \approx 0.6$ (dashed line in the inset). However, we should stress that the data are also compatible with the behavior $S_A \sim t^{1/2} |\log(t)|$ (dashed-dotted line in the inset). A similar power-law increase of the entanglement entropy has been observed in quantum quenches in quasicrystals [103]. Interestingly, partial revivals of the short-time dynamics are superposed with the power-law growth, in contrast with the local quench, where perfect revivals occur, apart from scaling corrections [23].

The qualitative behavior of the entanglement can be understood in a semiclassical picture in terms of the ballistic propagation of the magnetization wavefront discussed in Sec. III. This is illustrated in Fig. 3 (b). The initial entanglement in-

crease at $t > 0$ corresponds to the two edges of the wavefront (red and blue lines in the figure) propagating with equal velocities in the two parts of the chain. At $t = t_s^*/2$ the two edges are reflected at the physical boundaries. Finally, at $t = t_s^*$, a crossing of the two edge trajectories occurs. Every crossing at the later times $t = kt_s^*, k \in \mathbb{N}$, is reflected in an sudden increase in the von Neumann entropy (Fig. 3 (a)). A similar semiclassical picture [104] holds in the case of a local quench [22], where the entanglement growth is associated with the propagation of two “localized” defects [24, 100, 101].

At $t > t_\ell^* \sim L_A^2/v_s$, i.e., after $\mathcal{O}(L_A)$ crossings of the wavefront edge trajectories, (cf. Fig. 3 (b)), the system reaches a steady state and the von Neumann entropy oscillates around a stationary value. We anticipate that, since the model is integrable [89], the steady state is different from a thermal state, although its entanglement entropy is *extensive* (cf. Sec. VI).

V. SHORT-TIME ENTANGLEMENT DYNAMICS

In this section we focus on the short-time entanglement dynamics (i.e., at $t \leq t_s^*$, cf. Fig. 3 (a)). Here, in particular, we provide an analytic expression, which accurately describes the von Neumann entropy dynamics at short times $t \lesssim t_s^* \equiv \min(2L_A/(\nu v_s), 2L_B/\nu)$. We motivate this formula based on heuristic arguments. This result holds irrespective of the quench aspect ratio ω (see Fig. 4 (a)), since the spreading of information between A and B is associated with the propagation of the two wavefront edges (cf. Fig. 3 (b)) and part B of the chain is prepared in the “vacuum” state.

Figure 4 shows $S_A(t)$ as a function of the rescaled time $\nu v_s t / (2L_A) \leq 1$. Data are exact numerical results for the

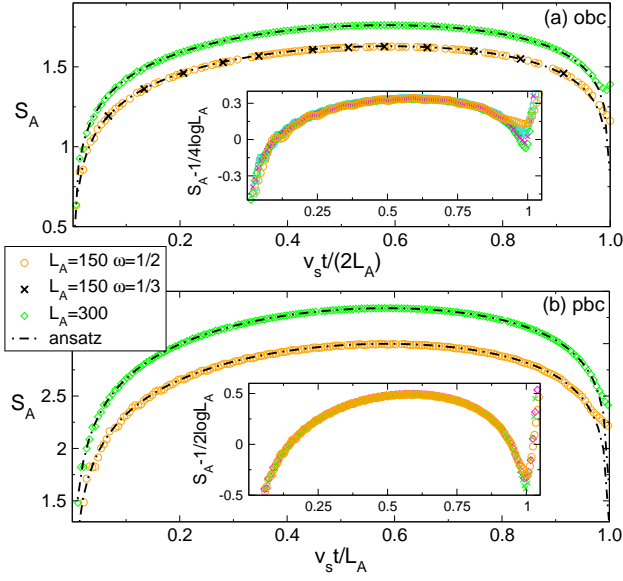


FIG. 4: von Neumann entropy S_A for part A after the geometric quench (with $\omega \equiv L_A/L = 1/2, 1/3$) in the XX chain: short-time behavior (at $t \leq t_s^* \sim L_A/v_s$, and $v_s = 1$ the spinon velocity). (a) XX chain with open boundary conditions, S_A versus $v_s t / (2L_A)$ (exact results for several sizes L_A). The crosses are data for $L = 150$ and $\omega = 1/3$. Dashed-dotted lines are one parameter fits to S_{ansatz} (see Eq. (12)). Inset: shifted entropy, $S_A - 1/4 \log L_A$ versus $v_s t / (2L_A)$. Note the perfect data collapse for all chain sizes and times. (b) The same as in (a) for periodic boundary conditions: now S_A is plotted versus $v_s t / L_A$. Dashed-dotted lines are fits to Eq. (12) (notice the dependence on boundary conditions). Inset: shifted entropy, $S_A - 1/2 \log L_A$ versus $v_s t / L_A$.

XX chain with either open or periodic boundary conditions (panels (a) and (b), respectively). For the sake of simplicity we restrict ourselves to a geometric quench with aspect ratio $\omega = 1/2$. Motivated by the result for the local quench [21, 23, 25, 27] Eq. (6) we have fitted the numerical data to

$$S_{\text{ansatz}}(t) = \alpha_\nu \log(t) + \beta_\nu \log \left[L_A \sin \frac{\nu \pi v_s t}{2L_A} \right] + \gamma_\nu \quad (11)$$

where $\nu = 1, 2$ are for open and periodic boundary conditions, respectively, $v_s = 1$ is the spinon velocity, and $\alpha_\nu, \beta_\nu, \gamma_\nu$ are fitting parameters. In Eq. (11) the first term is motivated by the fact that $S_A(t)$ is not symmetric under $t \rightarrow 2L_A/(\nu v_s) - t$, i.e., left-right inversion (see Fig. 4), while the second one is similar to the local quench result Eq. (6). We have numerically found that $\beta_\nu = 2\alpha_\nu = \nu/6$. Finally, we rewrite Eq. (11) as

$$S_{\text{ansatz}}(t) = \frac{\nu}{6} \log \left| L_A^{\frac{3}{2}} \left(\frac{\nu v_s t}{2L_A} \right)^{\frac{1}{2}} \sin \frac{\nu \pi v_s t}{2L_A} \right| + k'_\nu, \quad (12)$$

with k'_ν a constant. In the limit $t/L_A \ll 1$ (short times), one obtains from Eq. (12)

$$S_A(t) = \frac{\nu}{4} \log t + k'_\nu, \quad (13)$$

which is different from the local-quench CFT result Eq. (8). A similar result is discussed in Ref. 105, where the ground-state

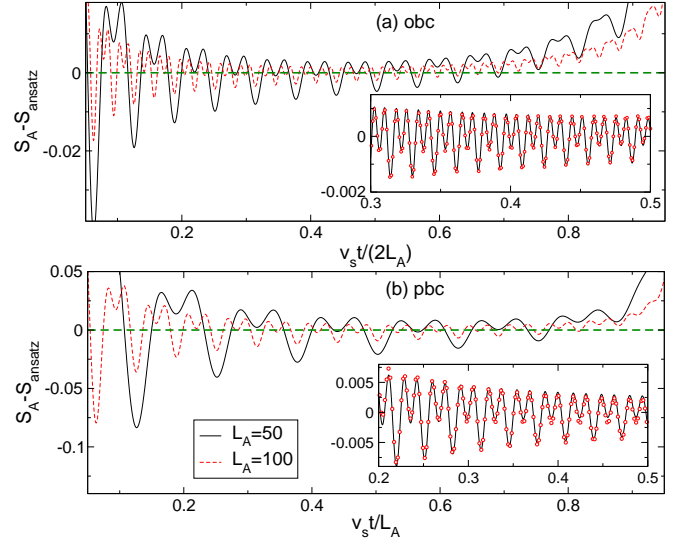


FIG. 5: Geometric quench ($\omega \equiv L_A/L = 1/2$, cf. Fig. 1) in the XX spin chain: short-time dynamics of the von Neumann entropy S_A for part A of the chain. Deviations from S_{ansatz} (see Eq. (12)) for (a) open and (b) periodic boundary condition. (a) $S_A - S_{\text{ansatz}}$ plotted versus $v_s t / (2L_A)$. Data are exact results for $L_A = 50, 100$ (full and dashed line, respectively). Note that k'_ν (see Eq. (12)) has been fitted and subtracted from the curves. Inset: same as in the main panel (circles are data for $L_A = 100$), the continuous line is a fit to $[a_1 \cos(t) + a_2 \cos(2t)]/t$. (b) Same as in (a) yet for periodic boundary conditions: $S_A - S_{\text{ansatz}}$ versus $v_s t / L_A$. Inset: same as in (a). The full line is a fit to $[a_1 \cos(t) + a_2 \cos(2t)]/t$.

entanglement entropy of two free-fermionic chains connected by a narrow “transition” region is studied. The two chains are completely full or empty, respectively, while a density variation in the transition region is induced by a linear chemical potential. Interestingly, the von Neumann entropy of a block that includes the transition region grows logarithmically with the block size, with a prefactor $1/4$, similar to Eq. (13).

It is useful to rewrite Eq. (12) as

$$S_{\text{ansatz}} = \frac{\nu}{6} \log \left| y^{\frac{1}{2}} \sin(\pi y) \right| + \frac{\nu}{4} \log(L_A) + k'_\nu, \quad (14)$$

with y being the rescaled time as in Eq. (6). Clearly, the shifted entanglement $S_A(t) - \nu/4 \log(L_A)$ is a function of only y .

The validity of Eq. (12) is further corroborated by comparing with the data shown in Fig. 4: dashed lines in the two panels (a) and (b) are one-parameter fits to Eq. (12), with k'_ν the only fitting parameter, which are in perfect agreement with the numerical results. In order to demonstrate the scaling behavior Eq. (14) we plot $S_A(t) - \nu/4 \log(L_A)$ versus $\nu v_s t / (2L_A)$ in the insets of Fig. 4. All data for different sizes collapse on the same curve, further confirming Eq. (12).

Finite-size deviations from Eq. (12) are illustrated in Fig. 5, plotting $S_A(t) - S_{\text{ansatz}}(t)$ versus $\nu v_s t / (2L_A)$ for $L_A = 50, 100$ (same data as in Fig. 4). The constant k'_ν (cf. Eq. (12)) has been fitted and subtracted from the data. Finite-size corrections oscillate with time and vanish in the limit of large

chains. We numerically checked that the formula

$$S_A(t) - S_{\text{ansatz}}(t) = \frac{1}{t} (a_1 \cos(t) + a_2 \cos(2t)) \quad (15)$$

accurately describes the corrections at the intermediate time scales $0 \ll t \ll L_A$, as shown in the inset in Fig. 5. Symbols are data for $L_A = 100$, while the continuous line is a fit to Eq. (15), with a_1, a_2 the fitting parameters. Notice the increasing behavior at $t \sim \nu L_A / v_s$, which could suggest a logarithmic correction as $\log(t)/t$. Similar corrections have been observed in the variance of the spin current after the quench from the “domain wall” state $|\cdots \uparrow\uparrow\downarrow\downarrow\cdots\rangle$ [102].

VI. ENTANGLEMENT PROPERTIES IN THE STEADY STATE

This section is devoted to studying entanglement properties in the steady state after a generic geometric quench with arbitrary aspect ratio ω (cf. Fig. 1). This corresponds to time scales $t \gg t_\ell^*$ (cf. Fig. 3 (c)). Here we restrict our analysis to the XX chain with periodic boundary conditions.

We first focus on the nature of the steady state after the quench. We show that it is *not* a thermal state, yet it reflects the initial half-filled Fermi sea in part A of the chain. This observation allows us to derive an approximate analytic expression for the steady-state entanglement entropy, which is then checked against exact numerical results, finding good agreement, at least in the limit $L_A \ll L$. Remarkably, despite the non-thermal nature of the state, its entanglement is *extensive*. This is also confirmed through direct inspection of the so-called single-particle entanglement spectrum (ES).

A. Non-thermal steady state

After a Jordan-Wigner transformation (cf. Appendix A) the XX Hamiltonian, obtained from Eq. (2) imposing $\Delta = 0$, is recast in a free-fermionic form as

$$\mathcal{H}_{XX} = -\frac{1}{2} \sum_{i=1}^{L-1} (c_i^\dagger c_{i+1} + c_i c_{i+1}^\dagger) \quad (16)$$

with c_i standard fermionic operators. Entanglement properties in free-fermionic models (cf. Appendix A) are fully characterized by the two-point correlation function $\mathbb{G}_{m,n} \equiv \langle c_m^\dagger c_n \rangle$ restricted to the subsystem, i.e., $m, n \in A$ [101, 106–110]. In the steady state, we numerically observe that the Fourier transform of $G_{m,n}$, $\tilde{\mathbb{G}}_{k,k'}$ is approximately diagonal, i.e., $\tilde{\mathbb{G}}_{k,k'} \approx n_k \delta_{k,k'}$, with n_k the subsystem momentum distribution function

$$n_k \equiv \langle c_k^\dagger c_k \rangle = \frac{1}{L_A} \sum_{m,n} e^{ik(m-n)} \langle c_m^\dagger c_n \rangle. \quad (17)$$

Here $k \equiv 2\pi s / L_A$, with $s = 0, 1, \dots, L_A - 1$, is the single-particle momentum, $\langle \cdot \rangle$ denotes the expectation value with the post-quench wavefunction at time t , and $m, n \in [1, L_A]$.

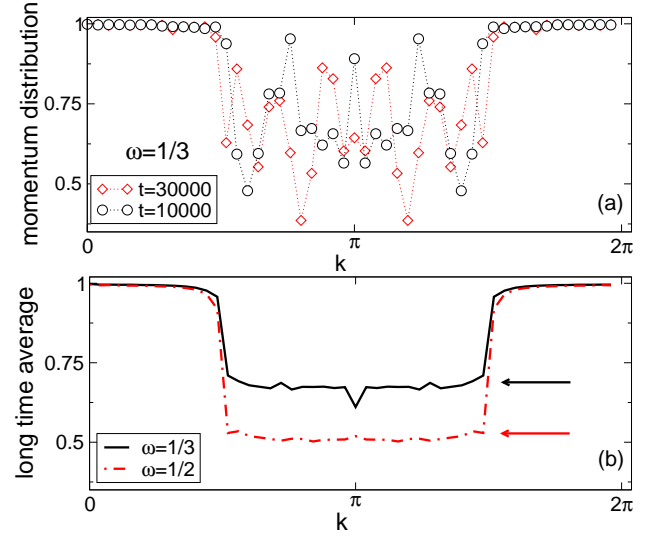


FIG. 6: Momentum distribution function $n_k \equiv \langle c_k^\dagger c_k \rangle$ restricted to part A of the chain (cf. Fig. 1) after a geometric quench in the periodic XX chain. Here c_k, c_k^\dagger are the fermionic operators of the corresponding free-fermion chain (cf. Appendix A). (a) n_k in the steady state ($t \gg t_\ell^*$, cf. Fig. 3) plotted versus the single-particle momentum $0 \leq k \leq 2\pi$. Data are for $L_A = 50$. (b) Long-time average of n_k (over the interval $20000 \leq t \leq 40000$). Full and dashed-dotted lines are for the geometric quench with aspect ratios $\omega = 1/3$ and $\omega = 1/2$, respectively (Fig. 1). The plateaux in the central region ($\pi/2 \leq k \leq 3\pi/2$) correspond to $n_k = 1 - \omega$ (arrows in the figure).

n_k is shown versus k in Fig. 6 (a). Data are for the XX chain with $L_A = 50$ and the geometric quench with aspect ratio $\omega = 1/3$. We restrict ourselves to times such that $t \gg t_\ell^*$ (cf. Fig. 3). Interestingly, apart from oscillations, a step-like structure is visible, which reflects the $t = 0$ half-filled Fermi sea in part A of the chain. The step-like form of n_k is better visible in Fig. 6 (b). The continuous and dashed-dotted lines denote the time-averaged n_k (in the interval $20000 \leq t \leq 40000$) for two different quenches with $\omega = 1/3$ and $\omega = 1/2$.

The form of n_k can be derived in a semiclassical framework. At $t = 0$ one can consider the excitations (particles) of the two independent chains A and B as uniformly distributed in each chain. Similarly, at $t \rightarrow \infty$ these are uniformly distributed in the final chain. Since the model is non-interacting, each mode preserves its momentum during the post-quench dynamics. The asymptotic (i.e., at $t \rightarrow \infty$) n_k is then obtained as the “average” of the two initial Fermi seas $n_k^0(A)$ and $n_k^0(B)$ of parts A and B , respectively. The result reads

$$n_k = \omega n_k^0(A) + (1 - \omega) n_k^0(B), \quad (18)$$

where $\omega = L_A/L$ and $1 - \omega = L_B/L_A$ have to be interpreted as the probabilities that a mode (with given momentum) is occupied by a particle originally in A and B , respectively. Notice that in the reasoning above we are considering $L, L_A \rightarrow \infty$, i.e., we neglect the finite lattice spacing. Using that $n_k^0(A)$ and $n_k^0(B)$ are the half-filled and the filled Fermi

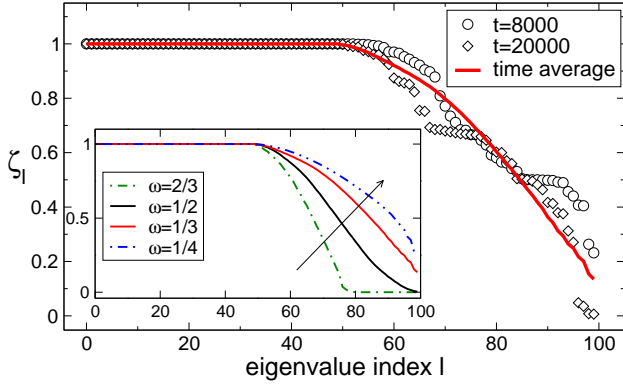


FIG. 7: Entanglement in the steady state after a geometric quench with $\omega = 1/3$ in the periodic XX chain. Single-particle entanglement spectrum levels ζ_l ($l = 1, 2, \dots, L_A$) at long times $t > t_\ell^*$ (see Fig. 3). Data are exact results for a chain with $L_A = 100$ and several times $8000 \leq t \leq 20000$. Note the first $L_A/2$ levels with $\zeta_l = 1$. The full line is the long time average. Inset: Long-time average of the single-particle entanglement spectrum for quench values of $\omega \equiv L_A/L = 2/3, 1/2, 1/3, 1/4$. The arrow indicates decreasing ω . Notice that the time averaged ζ_l are in general different from the time averaged n_k in Fig. 6 (b).

seas, respectively, one obtains

$$n_k = 1 - \omega \theta \left[k - \frac{\pi}{2} \right] \theta \left[\frac{3}{2}\pi - k \right], \quad (19)$$

in perfect agreement with the numerical data in Figs. 6 (a) and (b). We should mention that similar results have been obtained studying the dynamics from the initial state $|m\rangle \otimes | - m\rangle$ in Ref. 33.

B. Steady-state entanglement

The entanglement entropy of subsystem A at any time can be given as (cf. Appendix B)

$$S_A(t) = - \sum_l [\zeta_l \log \zeta_l + (1 - \zeta_l) \log(1 - \zeta_l)], \quad (20)$$

where ζ_l , which are related to the single-particle entanglement spectrum (ES) (cf. Appendix B), are the eigenvalues of the two-point correlation matrix $\mathbb{G}_{m,n}$ restricted to part A of the chain.

The behavior of ζ_l in the steady state is illustrated in Fig. 7 for the geometric quench with $\omega = L_A/L = 1/3$ and fixed $L_A = 100$. The continuous line is the (long) time average of the levels. At time $t > t_\ell^*$ there are $L_A/2$ (i.e., half of the levels) with $\zeta_l = 1$, which do not contribute to the entropy (cf. Eq. (20)). The remaining $L_A/2$ are distributed over the whole interval $(0, 1)$. The existence of an extensive number of levels with $\zeta_l \sim 1/2$ suggests that $S_A(t)$ is *extensive* in the steady state. This is dramatically different in the equilibrium ground state, where only few levels of the single-particle entanglement spectrum contribute in Eq. (20) (cf. Fig. 13 in Appendix B).

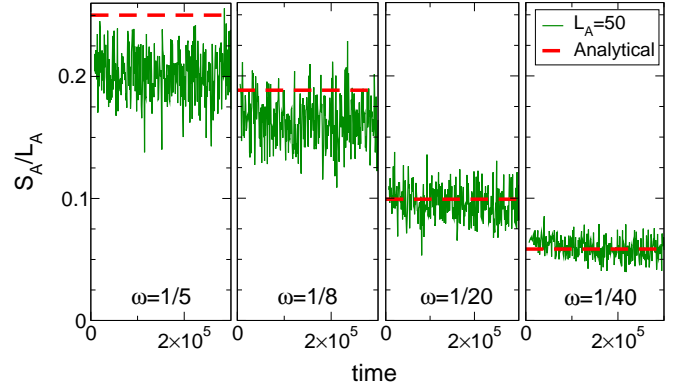


FIG. 8: Extensive entanglement in the steady state after a geometric quench. Data are for the periodic XX chain. von Neumann entropy S_A for part A of the chain (cf. Fig. 1) at large times ($t \gg t_\ell^*$, see Fig. 3): S_A/L_A plotted versus time t for quenches with several aspect ratios $\omega = L_A/L = 1/5, 1/8, 1/20, 1/40$ and $L_A = 50$ (the same scale is used on both axis in all the panels). The dashed line is $S_A/L_A = -[\omega \log \omega + (1 - \omega) \log(1 - \omega)]/2$.

The behavior of ζ_l upon varying the aspect ratio ω is illustrated in the inset in Fig. 7, showing the time-averaged levels for $\omega = 2/3, 1/2, 1/3, 1/4$. Irrespective of ω an extensive fraction ($\sim L_A/2$) of levels is in the region $\zeta_l \approx 1$. Moreover, as ω decreases the whole distribution is shifted towards $\zeta_l = 1$, signaling that, although extensive behavior persists at any ω , the actual value of the entropy decreases as $\omega \rightarrow 0$.

Finally, the scenario outlined above can be justified using Eq. (19), i.e., neglecting the oscillations in Fig. 6 (a). Within this approximation, $\mathbb{G}_{m,n}$ has $L_A/2$ identical eigenvalues $\zeta_l = 1 - \omega$ (and $L_A/2$ unit eigenvalues). Notice that these are different from the long time average of ζ_l in Fig. 7, suggesting that the diagonal approximation $\tilde{\mathbb{G}}_{k,k'} \approx n_k \delta_{k,k'}$ might be too crude. The von Neumann entropy, using Eq. (20) is then

$$\frac{S_A}{L_A} = -\frac{1}{2} [\omega \log \omega + (1 - \omega) \log(1 - \omega)]. \quad (21)$$

The comparison between Eq. (21) and the exact data is shown in Fig. 8, focusing on the geometric quenches with $\omega = 1/5, 1/8, 1/20, 1/40$ (panels from left to right in the figure). The continuous lines are data for S_A/L_A at fixed $L_A = 50$ and $10^4 < t < 10^6$. Clearly, $S_A/L_A \rightarrow 0$ upon decreasing ω , as expected (cf. inset in Fig. 7). In each panel, the value according to Eq. (21) is shown as a dashed line. At $\omega = 1/5$ and $\omega = 1/8$ some deviations from Eq. (21) are observed, which have to be interpreted as finite-size effects, due to the fact that $L_A \sim L$. In the limit $L_A \ll L$ (equivalent to $\omega \rightarrow 0$), Eq. (21) is in remarkably good agreement with the exact data.

It is interesting to investigate the entanglement fluctuations in the steady state. These are illustrated in Fig. 9 plotting the rescaled von Neumann entropy S_A/L_A versus t/L_A^2 . Data are for the open XX chain with $L = 100, 200, 400$ and a geometric quench with aspect ratio $\omega = 1/2$ (cf. Fig. 1). Here we focus on intermediate and long time scales after the quench, i.e., $t \gg t_s^*$ (see Fig. 3). Remarkably, in Fig. 9 all the data

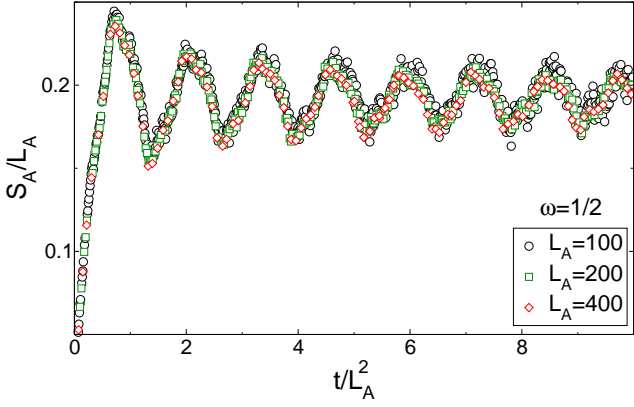


FIG. 9: Fluctuations of the entanglement entropy in the steady state after a geometric quench with aspect ratio $\omega \equiv L_A/L = 1/2$. Data are for the open XX chain with $L = 100, 200, 400$: rescaled von Neumann entropy S_A/L_A plotted versus the rescaled time t/L_A^2 . Notice that partial revivals (oscillations) persist in the long time regime, and do not decay with the chain size.

collapse on the same curve, confirming that the steady state exhibits extensive entanglement, in agreement with the semi-classical result Eq. (21). However, oscillating deviations from the steady state value are observed, with period $\sim 1/L_A^2$ and amplitude $\sim L_A$. Notice that at fixed t/L_A^2 these oscillations do not vanish in the limit $L_A \rightarrow \infty$.

VII. ENTANGLEMENT RELAXATION AFTER THE INFINITE CHAIN QUENCH

In this section we discuss the real-time entanglement dynamics after the infinite-chain geometric quench, which corresponds to the limit $\omega \rightarrow 0$, at fixed *finite* L_A (see Fig. 1). Here we focus on time scales $t > t_s^*$ (for $t < t_s^*$, one has the same behavior as in Sec. V), considering the XX chain with periodic boundary conditions. Although we are interested in the limit $\omega \rightarrow 0$, in practice we consider finite (large) ω restricting ourselves only to $t < L - L_A = L_A(\omega^{-1} - 1)$, to avoid reflections at the boundaries of the chain.

First, one has $S_A(t) \rightarrow 0$ at $t \rightarrow \infty$, since the wavefunction becomes a product state in the limit $\omega \rightarrow 0$. However, the entanglement relaxation dynamics, at any time $t > t_s^*$, is described by a scaling function $f_\ell(z)$ of the rescaled time $z = t/L_A^2$. Additionally, two different dynamical regimes appear: while $f_\ell(z) \sim -\log(z)$ at $z \lesssim 1$, a crossover to $f_\ell(z) \sim 1/z + 1/z \log(z)$ occurs around $z \sim 1$. The latter behavior can be calculated analytically.

All these features are present in the data shown in Fig. 10, plotting $S_A(t)$ versus $z \equiv t/L_A^2$ for a geometric quench with $\omega = 1/30$ and several L_A . The perfect data collapse provides robust evidence that the entanglement dynamics at $t > t_s^*$ is described by a scaling function $f_\ell(z)$. The behavior of $f_\ell(z)$ at $z \rightarrow \infty$ is given analytically as (cf. Appendix E)

$$S_A(t) \approx \frac{L_A^2}{2\pi t} \left[1 - \log \frac{L_A^2}{2\pi t} \right]. \quad (22)$$

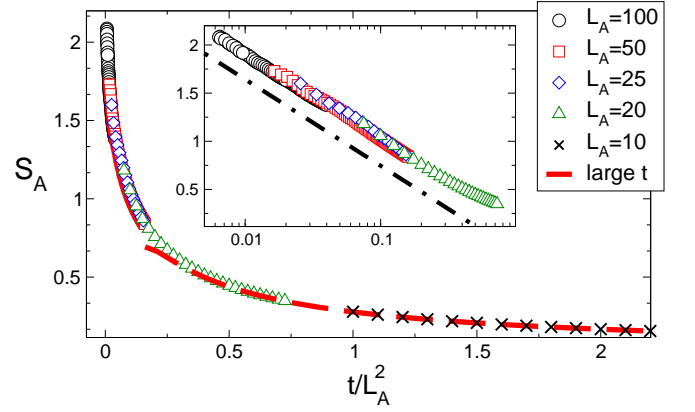


FIG. 10: Entanglement relaxation after the geometric quench with aspect ratio $\omega \equiv L_A/L \ll 1$ in the periodic XX chain. Symbols are exact numerical data for $L_A = 10, 20, 25, 50, 100$. Rescaled entropy dynamics: S_A versus t/L_A^2 . Perfect data collapse is observed for all L_A and times. The dashed line is the analytic result at $t \rightarrow \infty$. Inset: same as in the main figure at $t/L_A^2 < 1$. Note the logarithmic scale on the x -axis. The dashed-dotted line is $-0.4 \log(t/L_A^2)$.

This is shown in Fig. 10 as a dashed line, in perfect agreement with the numerical data already at $t/L_A^2 \sim 1/2$. On the other hand, at $t/L_A^2 \ll 1$, one has the strikingly different behavior $S_A(t) = -\alpha \log(t/L_A^2) + \beta$, as numerically demonstrated in the inset of Fig. 10. In particular, a fit of the numerical data gives $\alpha \approx 0.4$ (dashed-dotted line in the figure).

VIII. GEOMETRIC QUENCH IN THE XXZ CHAIN

We now turn to the post-quench dynamics in interacting models, considering the XXZ chain in the gapless phase at $-1 < \Delta \leq 1$. We restrict ourselves to short time scales, which can be accessed efficiently using tDMRG [77, 78, 93, 94].

We provide numerical evidence that qualitative and quantitative features are similar to the XX chain. First, after the quench a magnetization wavefront forms, spreading ballistically in the two parts of the chain A and B (cf. Fig. 1). However, while in the XX chain the two wavefront edges propagate with the same velocity (i.e., $v = 1$, see Sec. III), here two different velocities appear. More precisely, the propagation in parts A and B happens at the spinon velocity $v_s(\Delta)$ and $v = 1$, respectively. Interestingly, we find that the central region of the wavefront is described by Eq. (10).

On the other hand, the entanglement dynamics is well described by the same formula derived for the XX chain (cf. Eq. (12)). However, as the wavefronts (and consequently the information) propagation is anisotropic in the two parts of the chain, a remarkable difference is that one has to replace $v_s \rightarrow v_e$ in Eq. (12), with v_e being an effective entanglement spreading rate. We numerically find that $v_e \approx v_s$ for $\Delta < 0$ (i.e., the entanglement spreads with the wavefront edge velocity), whereas one has $v_e < v_s$ at $\Delta > 0$.

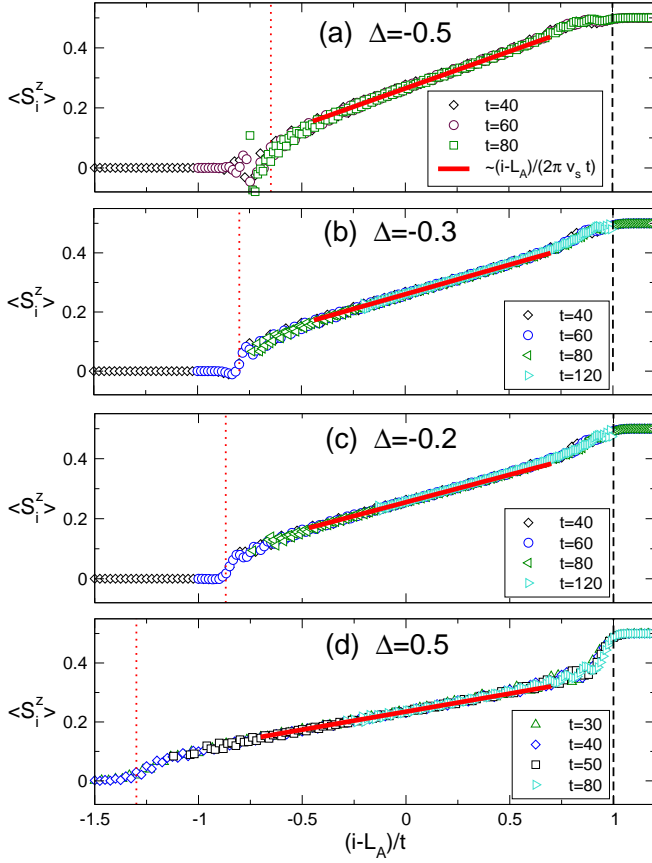


FIG. 11: Magnetization wavefront after a geometric quench with aspect ratio $\omega \equiv L_A/L = 1/3$ in the XXZ spin chain. Symbols are tDMRG data for $L_A = 60$ and anisotropies $\Delta = -0.5, -0.3, -0.2, 0.5$ (panels (a)-(d) in the figure). The same scale is used on the x -axis in all panels. The local magnetization $\langle S_i^z \rangle$ is plotted versus $(i - L_A)/t$, with i being the position in the chain. All the data collapse on the same Δ dependent scaling function. The dashed vertical line corresponds to $(i - L_A)/t = 1$, while the dashed-dotted one is $(i - L_A)/t = -v_s(\Delta)$, with $v_s(\Delta)$ the spinon velocity. The continuous lines are fits to $s_0 + (i - L_A)/(2\pi v_s(\Delta)t)$, with $s_0 \approx 1/4$ the fitting parameter.

A. Ballistic wavefront propagation

The local magnetization $\langle S_i^z(t) \rangle$ as a function of the site position i in the chain is shown in Fig. 11 for several times after the geometric quench. We restrict ourselves to $\omega = 1/3$, showing data at fixed $L_A = 60$ and several values of the anisotropy Δ in the spin-liquid phase ($\Delta = -0.5, -0.3, -0.2, 0.5$, panels (a)-(d) in the figure). Symbols denote tDMRG data for an XXZ chain with open boundary conditions and $t \ll L_A$ to avoid effects from reflections at the boundary of the chain.

The formation of two propagating wavefronts at $t > 0$ is clearly visible for all values of Δ . Their left and right edges propagate ballistically in the two parts of the chain (see also Ref. 79, 111). This is illustrated plotting $\langle S_i^z \rangle$ versus the rescaled variable $(i - L_A)/t$. At each Δ , the data collapse on the same function for all times and positions.

The vertical dashed-dotted line in Fig. 11 marks the point $(i - L_A)/t = -v_s$. For the XXZ chain in the zero magnetization sector v_s is given as [112]

$$v_s(\Delta) = \frac{\pi \sin \gamma}{2 \gamma} \quad \text{with} \quad \cos \gamma = \Delta. \quad (23)$$

Clearly, $\langle S_i^z \rangle = 0$ at $(i - L_A)/t = -v_s$, demonstrating that the left edge of the wavefront propagates with v_s . On the other hand, the right one propagates at unit velocity (the dashed lines in all panels mark the point $(i - L_A)/t = 1$). Although the full scaling function $\langle S_i^z \rangle \equiv m((i - L_A)/t)$ is not easily accessible, at $(i - L_A) \ll t$ (central region in the panels in Fig. 11) the magnetization profile exhibits the linear behavior $\langle S_i^z \rangle \sim (i - L_A)/t$. It is reasonable that this is given analytically by (as a generalization of Eq. (10))

$$\langle S_i^z \rangle \approx s_0 + \frac{i - L_A}{2\pi v_s(\Delta)t}. \quad (24)$$

The validity of Eq. (24) is confirmed in Fig. 11. Continuous lines in the figure are fits to Eq. (24) (with $s_0 \approx 1/4$ the fitting parameter), and are in excellent agreement with the tDMRG data.

B. Short-time entanglement dynamics

In this section we investigate the entanglement spreading after a geometric quench in the (open) XXZ chain in the gapless phase (i.e., $-1 < \Delta \leq 1$). At short time scales that can be accessed by tDMRG it is natural to generalize the result at $\Delta = 0$ (cf. Eq. (12)) as

$$S_{\text{ansatz}}(t) = \frac{\nu}{6} \log \left[L_A^{\frac{3}{2}} \left(\frac{\nu v_e t}{2L_A} \right)^{\frac{1}{2}} \sin \frac{\nu \pi v_e t}{2L_A} \right] + k'_\nu \quad (25)$$

with $\nu = 1$ for open and $\nu = 2$ for periodic boundary conditions, k'_ν a Δ -dependent constant, and v_e an entanglement spreading rate. Equation (25) is expected to hold at $t \ll 2L_B$, although we are not able to provide its precise regime of validity, which would require the exact expression for v_e . From Eq. (25) one finds that $S_A(t) - \nu/4 \log(L_A)$ is a scaling function of t/L_A . The validity of Eq. (25) is shown in Fig. 12, considering tDMRG data for the XXZ chain at $\Delta = -1/2$ (panel (a) in the figure) and $\Delta = 1/2$ (panel (b)). We provide data for $L_A = 20, 30, 40, 60$, restricting ourselves to a geometric quench with $\omega = 1/3$. Strikingly, all the data for different system sizes collapse on the same scaling curve, in agreement with Eq. (25). To further proceed we fit the data to Eq. (25) (k'_ν and v_e being the only fitting parameters). Remarkably, at $\Delta = -1/2$, we obtain $v_e \approx v_s$ (the vertical dotted line in Fig. 12 marks the point at $2L_A/t = v_s$). Also, we numerically verified that $v_e \approx v_s$ in the whole interval $-1 < \Delta \leq 0$. However, at $\Delta = 1/2$ we obtain $v_e \approx 1.13 < v_s \approx 1.3$ (the vertical-dashed line in Fig. 12 marks the point $t/(2L_A) = 1/v_s$). Our analysis suggests that although the information spreading between the two parts A and B of the chain is associated with the wavefront propagation, the spreading rate v_e is not a trivial function of the wavefront edges' velocities.

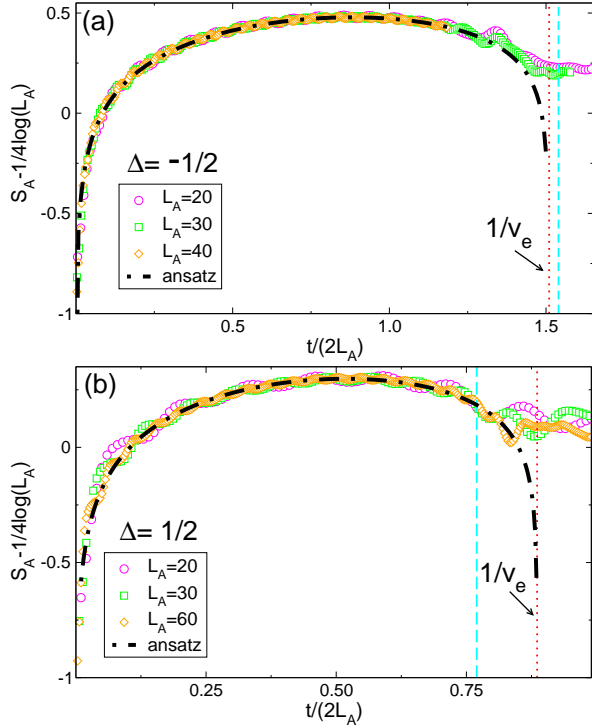


FIG. 12: Entanglement spreading after the geometric quench with aspect ratio $\omega \equiv L_A/L = 1/3$ (see Fig. 1) in the XXZ spin chain at $\Delta = -1/2$ (a) and $\Delta = 1/2$ (b). (a) Shifted von Neumann entropy $S_A - 1/4 \log L_A$ versus $t/(2L_A)$. Symbols are tDMRG data for $L_A = 20, 30, 40$. Notice the perfect data collapse for all sizes and times. The dashed line are fits to S_{ansatz} (Eq. (25)), with v_e (entanglement spreading rate) and k'_ν the fitting parameters. The vertical dotted line marks the point $2L_A/t = v_e$. The fit gives $v_e \approx v_s(\Delta)$. (b) Same as in (a) for $\Delta = 1/2$ and $L_A = 20, 30, 60$. The fit to Eq. (25) now yields $v_e \approx 1.13 < v_s \approx 1.3$. In both panels, the vertical dashed line is $1/v_s(\Delta)$.

IX. SUMMARY AND CONCLUSIONS

In this work we investigated the entanglement dynamics after a geometric quench in the XXZ chain in the gapless phase, both analytically and numerically. The initial state after the quench is obtained joining two chains A and B , of lengths L_A and L_B , prepared in the ground state of the XXZ chain in the sector with zero and maximum magnetization, respectively. The latter is the fully polarized state, which can be a high-energy eigenstate of the model, depending on the exchange anisotropy. Equivalently, in the language of interacting fermions confined in a hard-wall trap, the geometric quench corresponds to a sudden change in the trap size. From the energy point of view, this quench falls into the class of global quenches, since the excess energy density above the ground state of the final Hamiltonian is finite. On the other hand, both A and B are in eigenstates of the XXZ model, implying that the post-quench dynamics originates locally from a “defect” at the interface between the two chains, as in typical local quenches.

The entanglement growth after the quench is associated

with the formation of a magnetization wavefront, whose edges propagate *ballistically* in the two parts of the chain, at different velocities. To be precise, while the wavefront expands in part A with the spinon velocity, in part B this happens at unit velocity. For the XX chain we derived the exact analytical expression of the wavefront profile using free-fermionic techniques and semiclassical arguments. For the XXZ model we found that the central region of the wavefront is described by a simple function, which depends on the spinon velocity.

Focusing on the XX chain we observed that the entanglement dynamics after the quench exhibits several interesting dynamical regimes. Specifically, at $t \leq t_s^* \sim L_A/v_s$ (short time scales) the von Neumann entropy increases logarithmically. Moreover, while the well-known CFT result [21–23] for the entanglement growth in local quenches does not apply, we provided an analytic formula, derived from heuristic arguments, that describes accurately the short-time entanglement dynamics. Remarkably, the entanglement entropy exhibits the scaling behavior $S_A(t) = f_s(y) + s(L_A)$, with $y = t/L_A$, $s(L_A) = \nu/4 \log(L_A)$ (here $\nu = 1, 2$ for open and periodic boundary conditions, respectively), and $f_s(y)$ a scaling function. At larger times ($t_s^* \leq t \leq t_\ell^*$, with $t_\ell^* \sim L_A^2/v_s$) the von Neumann entropy shows partial revivals of the short-time dynamics superposed with a power-law increase $S_A \sim t^\alpha$. We numerically found $\alpha < 1$.

At very long times $t \geq t_\ell^*$ the system reaches a steady state and the entanglement entropy saturates, apart from oscillations. As expected, since the model is integrable, the steady state is *not* thermal. More precisely, we observed that the subsystem momentum distribution function shows discontinuities at $k = \pi/2$, reflecting the initial half-filled Fermi sea in part A of the chain. Finally, we provided numerical and analytical evidence that the steady-state entanglement is *extensive*.

We also considered the geometric quench from a finite to the infinite chain. While at large times one has $S_A \rightarrow 0$, reflecting the wavefunction being an almost perfect product state, the entanglement relaxation dynamics exhibits the scaling form $S_A(t) = f_\ell(z)$, with $z \equiv t/L_A^2$. Interestingly, the behavior of $f_\ell(z)$ changes dramatically at $z \sim 1$ (i.e., $t \sim L_A^2$). Namely, we numerically observed that $f_\ell(z) \approx -\gamma \log(z)$, with $\gamma \approx 0.4$ at $z \lesssim 1$. On the other hand, at $z \gtrsim 1$ we derived analytically $f_\ell(z) \approx 1/z(1 - \log(1/z))$.

Finally, by means of tDMRG simulations we discussed the role of interactions in the short-time entanglement dynamics, considering the XXZ chain in the gapless phase $-1 < \Delta \leq 1$. Interestingly, we numerically demonstrated that the same formula conjectured for the free-fermion case fully reproduces the short-time entanglement dynamics after the quench. Due to the anisotropic propagation of the wavefront in the two parts of the chain A and B , the entanglement spreading rate is not trivially related to the velocity of a single wavefront edge.

X. ACKNOWLEDGEMENTS

We acknowledge very fruitful discussions with J.-S. Caux, P. Calabrese, M. Fagotti, M. Haque, J. Mossel, G. Palacios,

P. Ribeiro. V.A. thanks J.-S. Caux, J. Mossel, and G. Palacios for valuable discussions in a related project, from which this work originated. We thank F. Iglói and J. H. H. Perk for useful comments on a previous version of the manuscript.

Appendix A: Diagonalization of the spin-1/2 XX chain

The spin-1/2 open XX chain [113–117] of length L in an external magnetic field h is defined as

$$\mathcal{H}_{XX} = -J \sum_{i=1}^{L-1} (S_i^x S_{i+1}^x + S_i^y S_{i+1}^y) + h \sum_{i=1}^L S_i^z, \quad (\text{A1})$$

with $S_i^{x,y,z} \equiv \sigma_i^{x,y,z}/2$, σ_i^α being the Pauli matrices acting on site i . For periodic boundary conditions one has an extra term in Eq. (A1) connecting site L with site 1. Hereafter we fix $J = 1$ for convenience. After the Jordan-Wigner transformation

$$c_i = \left(\prod_{m=1}^{i-1} \sigma_m^z \right) \frac{\sigma_i^x - i\sigma_i^y}{2}, \quad (\text{A2})$$

Eq. (A1) is recast in the free-fermionic form

$$\mathcal{H}_{XX} = -\frac{1}{2} \sum_{i=1}^{L-1} (c_i^\dagger c_{i+1} + c_i c_{i+1}^\dagger) + \frac{h}{2} \sum_{i=1}^L c_i^\dagger c_i, \quad (\text{A3})$$

with c_i spinless fermionic operators satisfying the canonical anticommutation relations $\{c_m, c_n^\dagger\} = \delta_{m,n}$. Notice in Eq. (A2) the non local term (Jordan-Wigner string) in the brackets. The mapping between Eq. (A1) and Eq. (A3) is exact apart from boundary terms (that we neglect here) giving a vanishing contribution (as $1/L$) to physical quantities in the large chain limit.

Periodic boundary conditions (pbc).— For periodic boundary conditions the spectrum of Eq. (A3) can be obtained going to momentum space. After defining the Fourier transformed operators c_k as

$$c_k = \frac{1}{\sqrt{L}} \sum_{m=1}^L e^{i\frac{2\pi k}{L}m} c_m, \quad (\text{A4})$$

and substituting in Eq. (A3), one obtains the single-particle dispersion E_k of the XX chain as

$$E_k = -\cos \frac{2\pi k}{L} + h \quad \text{with} \quad k = 0, 1, \dots, L-1, \quad (\text{A5})$$

with $2\pi k/L$ and E_k the single-particle momenta and energies, respectively. The single-particle eigenstate $|v_k\rangle$ corresponding to the eigenvalue E_k reads

$$|v_k\rangle = \frac{1}{\sqrt{L}} \sum_{m=1}^L e^{i\frac{2\pi k}{L}m} c_m^\dagger |0\rangle, \quad (\text{A6})$$

with $|0\rangle$ denoting the vacuum state for the fermions.

Open boundary conditions (obc).— For the XX chain with open boundary conditions one has instead

$$E'_k = -\cos \frac{\pi k}{L+1} + h \quad \text{with} \quad k = 0, 1, \dots, L-1, \quad (\text{A7})$$

while the single-particle eigenstates are

$$|v'_k\rangle = \sqrt{\frac{2}{L+1}} \sum_{m=1}^L \sin \left[\frac{\pi m k}{L+1} \right] c_m^\dagger |0\rangle. \quad (\text{A8})$$

The spectrum of the model (cf. Eq. (A5) and Eq. (A7)) is gapless in the thermodynamic limit at $|h| < 1$, while it is gapped otherwise. The ground state at $h = 1$ ($h = -1$) corresponds to an empty (fully filled) band.

The ground state of the XX chain is obtained by filling the single-particle levels (cf. Eqs. (A5) and (A7)) below the Fermi level $k_F = L/(2\pi) \cos^{-1}(h)$ and $k_F = (L+1)/\pi \cos^{-1}(h)$ for periodic and open boundary conditions, respectively. Notice that for convenience, the Fermi level k_F is defined as an integer. In this work we restrict ourselves to the XX chain with zero magnetic field ($h = 0$).

Appendix B: Entanglement entropies in free-fermionic chains

Here we briefly review how to calculate the entanglement entropy for a generic eigenstate of a free-fermionic model [101, 106–110, 118], focusing, in particular, on the ground-state entropy. The von Neumann entropy (and Renyi entropies as well) of a *single* interval $A \equiv [1, L_A]$ (of length L_A) embedded in a free-fermionic chain can be obtained from the two-point correlation function $\mathbb{G}_{m,n}$ restricted to the subsystem A

$$\mathbb{G}_{m,n} = \langle c_m^\dagger c_n \rangle \quad \text{with} \quad m, n = 1, 2, \dots, L_A. \quad (\text{B1})$$

Here $\langle \cdot \rangle$ denotes the expectation value over a generic eigenstate of Eq. (A3).

Ground-state correlation matrix.— The correlation matrix $\mathbb{G}_{m,n}$ (cf. Eq. (B1)) for a generic eigenstate of Eq. (A3) can be obtained using the explicit form of the single-particle eigenvectors Eq. (A6) and Eq. (A8). For the ground state of Eq. (A3) and periodic boundary conditions one obtains

$$\mathbb{G}_{m,n}^{(\text{pbc})} = \frac{2}{L} \sum_{k=0}^{L/4-1} \cos \left[\frac{2\pi(m-n)k}{L} \right] - \frac{1}{L}. \quad (\text{B2})$$

Performing the summation over k one obtains

$$\mathbb{G}_{m,n}^{(\text{pbc})} = \frac{1}{L} \frac{\sin \left[\left(\frac{\pi}{2} - \frac{\pi}{L} \right) (m-n) \right]}{\sin \left[\frac{\pi}{L} (m-n) \right]}. \quad (\text{B3})$$

In the limit of an infinite chain, Eq. (B3) reduces to

$$\mathbb{G}_{m,n}^{(\text{pbc})} (L \gg 1) \rightarrow \frac{\sin \left[\frac{\pi}{2} (m-n) \right]}{\pi (m-n)}. \quad (\text{B4})$$

Finally, for open boundary conditions $\mathbb{G}_{m,n}^{(\text{obc})}$ reads

$$\mathbb{G}_{m,n}^{(\text{obc})} = \frac{1}{2(L+1)} \left[\frac{\sin \frac{\pi}{2}(m-n)}{\sin \frac{\pi}{2(L+1)}(m-n)} - \frac{\sin \frac{\pi}{2}(m+n)}{\sin \frac{\pi}{2(L+1)}(m+n)} \right]. \quad (\text{B5})$$

For free-fermionic models the reduced density matrix for A can be written as

$$\rho_A = \frac{1}{Z} \exp(-\mathcal{H}_E) \quad (\text{B6})$$

where Z ensures the normalization $\text{Tr} \rho_A = 1$, and \mathcal{H}_E is the so-called entanglement Hamiltonian. The spectrum of the reduced density matrix ρ_A in Eq. (B6), which is expressed in the free-fermionic variables c_i , coincides with that of the reduced density matrix of the same block A expressed in the original spin variables $\sigma_i^{x,y,z}$. Since the Jordan-Wigner transformation Eq. (A2) is non-local, this is a non-trivial fact, and it rests on subsystem A being a single interval. In fact, it does not remain true for two (or many) disjoint intervals [119–124].

The spectrum of \mathcal{H}_E (single-particle entanglement spectrum) is of the free-type, reflecting the original Hamiltonian Eq. (A3) being quadratic, and its single-particle levels ϵ_l (l being an arbitrary label) are obtained from the eigenvalues ζ_l of $\mathbb{G}_{m,n}$ (cf. Eq. (B1)) as

$$\epsilon_l = \log \left[\frac{1 - \zeta_l}{\zeta_l} \right]. \quad (\text{B7})$$

Finally, the von Neumann entropy S_A of A is obtained as

$$S_A = \sum_{l=1}^{L_A} \left[\log(1 + e^{-\epsilon_l}) + \frac{\epsilon_l}{1 + e^{\epsilon_l}} \right]. \quad (\text{B8})$$

Equivalently, in terms of ζ_k one can write

$$S_A = \sum_{l=1}^{L_A} [\zeta_l \log \zeta_l - (1 - \zeta_l) \log(1 - \zeta_l)]. \quad (\text{B9})$$

It is noteworthy that the term in the sum in Eq. (B9) has a maximum at $\zeta_l = 1/2$, whereas it is vanishing for $\zeta_l = 0, 1$.

An example of a single-particle entanglement spectrum is shown in Fig. 13 plotting the eigenvalues ζ_l for a periodic XX chain with $L = 300$ and block A with $L_A = 75$ and $L_A = 150$ (rhombi and circles in the figure, respectively). Clearly, a large fraction of the spectrum (levels with $\zeta_l = 0, 1$) does not contribute to the entanglement entropy (cf. Eq. (B9)).

Appendix C: Entanglement entropies after a geometric quench

In this section we illustrate the calculation of the entanglement entropy at *any* time after a generic (i.e., with arbitrary aspect ratio ω , see Fig. 1) geometric quench in the XX chain. Similar results can be obtained for the 1D XY model (see Refs. [114–117]) or the transverse-field Ising chain (see

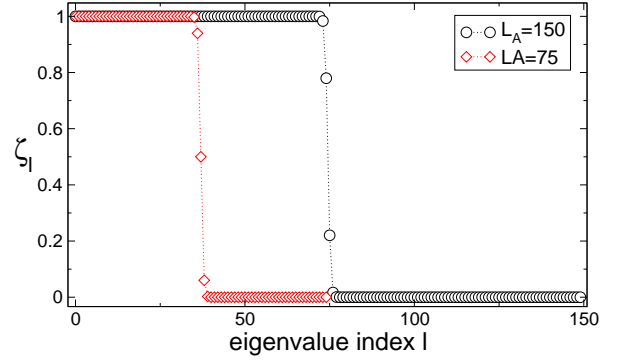


FIG. 13: Ground-state single-particle entanglement spectrum (ES) levels for the XX chain. Symbols are exact results for a chain of length $L = 300$. The ES levels are for a subsystem with $L_A = 75$ (rhombi) and $L_A = 150$ (circles). Only few ES levels (with $\zeta_l \neq 0, 1$) contribute to the entanglement entropy.

Refs [125, 126 and references therein). For simplicity, here we consider the situation in which both the initial chain A (see Fig. 1) and the final one have periodic boundary conditions. Notice that this implies that the quench protocol (see Fig. 1) involves a “cut and glue” step.

At $t = 0$ the initial state of the XX chain is obtained by gluing together the zero-magnetization ground state of a chain of length L_A with a fully-polarized state $|F\rangle \equiv |\uparrow\uparrow\uparrow \cdots \uparrow\rangle$ of length $L_B \equiv L - L_A$. The two-point correlation matrix $\mathbb{G}_{m,n}(t)$ at $t = 0$ is given as

$$\mathbb{G}_{m,n}(0) = \begin{cases} \mathbb{G}_{m,n}^{(\text{init})} & \text{if } (m,n) \in A \\ \delta_{m,n} & \text{otherwise} \end{cases} \quad (\text{C1})$$

with $\mathbb{G}_{m,n}^{(\text{init})}$ the $t = 0$ correlation function in part A of the chain, and $\delta_{m,n}$ the Kronecker delta. Here we choose $\mathbb{G}_{m,n}^{(\text{init})} = \mathbb{G}_{m,n}^{(\text{pbc})}$ (Eq. (B3) after replacing $L \rightarrow L_A$). At $t > 0$ after the quench $\mathbb{G}_{m,n}(t)$ is obtained as follows. One first defines $U_{kj} \equiv \sum_m R_{km} e^{iE_m t} (R^\dagger)_{mj}$, where R_{kj} is constructed as $R_{kj} \equiv \langle 0|c_j|v_k\rangle$ and E_m is given by Eq. (A5). One then has

$$\mathbb{G}(t) = U^\dagger \mathbb{G}(0) U. \quad (\text{C2})$$

The explicit expression after performing the matrix multiplications in Eq. (C2) reads

$$\mathbb{G}_{m,n}(t) = \sum_{k,k'} e^{-2\pi i \frac{k}{L} m + 2\pi i \frac{k'}{L} n + i(E_{k'} - E_k)t} \left[\frac{1}{L} \delta_{kk'} - \frac{1}{L^2} \frac{1}{L_A} \sum_{r=-k_F}^{k_F} \frac{1 - e^{2\pi i \omega k}}{1 - e^{i \frac{2\pi}{L_A}(r+\omega k)}} \times \frac{1 - e^{-2\pi i \omega k'}}{1 - e^{-i \frac{2\pi}{L_A}(r+\omega k')}} \right]. \quad (\text{C3})$$

It is convenient to define the matrix $\mathbb{F}_{r,m}(t)$ as

$$\mathbb{F}_{r,m}(t) \equiv \frac{1}{L} \sum_k e^{-2\pi i \frac{k}{L} m - iE_k t} \frac{1 - e^{2\pi i \omega k}}{1 - e^{i \frac{2\pi}{L_A}(r+\omega k)}}. \quad (\text{C4})$$

Thus one can rewrite Eq. (C3) in the form

$$\mathbb{G}_{m,n}(t) = \delta_{m,n} - \frac{1}{L_A} \sum_{r=-k_F}^{k_F} \mathbb{F}_{m,r}(t) \mathbb{F}_{n,r}^*(t). \quad (\text{C5})$$

Finally, the entanglement entropy for part A of the chain after the geometric quench is obtained from the eigenvalues of Eq. (C5) restricted to A , using Eq. (B9).

Appendix D: Dynamics after quenching to the infinite chain

In this section we focus on the entanglement dynamics after a geometric quench in the limit $\omega \rightarrow 0$ (quench to the infinite chain, cf. Fig. 1). Notice that the limit $\omega \rightarrow 0$ is taken at fixed finite L_A .

The time evolved correlation function $\mathbb{G}_{m,n}(t)$ has the same form as in Eq. (C5) after redefining $\mathbb{F}_{m,r}(t)$ as

$$\mathbb{F}_{m,r}(t) = \frac{1}{2\pi} \int_0^{2\pi} dk \frac{1 - e^{iL_A k}}{1 - e^{i\frac{2\pi r}{L_A} + ik}} e^{-imk + it \cos k}. \quad (\text{D1})$$

One should observe that in the limit $L_A \gg 1$, the second term in the numerator in Eq. (D1) is highly oscillating and one can write

$$\mathbb{F}_{m,k_s}(t) \xrightarrow{L_A \gg 1} \frac{1}{2\pi} \mathcal{P} \int_0^{2\pi} dk \frac{e^{-imk + it \cos k}}{1 - e^{i(k+k_s)}} + \frac{1}{2} e^{imk + it \cos k_s} \quad (\text{D2})$$

where \mathcal{P} denotes the Cauchy principal value of the integrand and we introduced $k_s \equiv 2\pi r/L_A$. The approximation Eq. (D2) holds provided that $m \ll L_A$, $t \ll L_A$, and $k_s \neq 0$.

A numerically more convenient expression is obtained writing

$$\mathbb{F}_{m,k_s}(t) = \sum_{p=0}^{L_A} e^{ipk_s + i(m-p)\frac{\pi}{2}} J_{p-m}(2t), \quad (\text{D3})$$

where $J_q(x)$ is the modified Bessel function. In the limit $L_A \rightarrow \infty$, using Eq. (C5), k_s becomes a continuous variable and one can write $\mathbb{G}_{m,n}(t)$ as

$$\mathbb{G}_{m,n}(t) = \delta_{m,n} - \frac{1}{2\pi} \int_{-\frac{\pi}{2}}^{\frac{\pi}{2}} dk_s \mathbb{F}_{m,k_s}(t) \mathbb{F}_{n,k_s}^*(t). \quad (\text{D4})$$

After using Eq. (D3) and performing explicitly the integration in Eq. (D4), $\mathbb{G}_{m,n}(t)$ reads

$$\mathbb{G}_{m,n}(t) = \delta_{m,n} - \sum_{p,q=0}^{L_A-1} \frac{\sin[\frac{1}{2}\pi(p-q)]}{\pi(p-q)} J_{p-m}(2t) J_{q-n}^*(2t) i^{m-p-n+q}. \quad (\text{D5})$$

Notice that we keep L_A finite in Eq. (D5), although formally the limit $L_A \rightarrow \infty$ is taken in Eq. (D4). It is convenient to

redefine $s = (p+q)/2$ and $d = (p-q)/2$ obtaining

$$\mathbb{G}_{m,n}(t) = \delta_{m,n} - \sum_{d=-L_A/2}^{L_A/2} \sum_{s=|d|}^{L_A-|d|} \frac{\sin \pi d}{2\pi d} J_{s+d-m}(2t) J_{s-d-n}^*(2t) i^{m-n-2d}. \quad (\text{D6})$$

Since $\sin(\pi d)/d$ is highly oscillating, in practice in Eq. (D5) it is possible to restrict the summation to the first few values of d . It is also worth reminding that $J_q(x)$ are exponentially vanishing at $|q| > x$, implying in Eq. (D6) that the contribution of the sum vanishes at $|s+d-m|/2 > t$ and $|s-d-n|/2 > t$, which is a manifestation of the Lieb-Robinson bound [127] in free models.

Appendix E: Some remarkable scaling properties at large times

In this section we derive the scaling form Eq. (22) for the von Neumann entropy at large times $t \rightarrow \infty$ after the quench from a finite to the infinite chain (cf. Appendix D).

The main ingredient of the calculation is the asymptotic behavior at $t \rightarrow \infty$ of the matrices $\mathbb{F}_{m,r}(t)$ (cf. Eq. (D1)). This is obtained using the stationary phase method [128]. The large-time behavior of $\mathbb{F}_{m,r}$ depends crucially on the parity of L_A and on the value of r .

In particular, for $r = 0$, irrespective of the parity of L_A , one obtains

$$\mathbb{F}_{m,0}(t) \approx \frac{\sqrt{2}}{\sqrt{\pi t}} \left[\frac{(-1)^m}{2} e^{it - i\frac{\pi}{4}} + L_A e^{-it + i\frac{\pi}{4}} \right], \quad (\text{E1})$$

where we neglect terms $\mathcal{O}(t^{-1})$. For generic $r \neq 0$ and odd L_A one has

$$\mathbb{F}_{m,r}(t) \approx (-1)^m \frac{e^{it}}{\sqrt{4\pi t}} \left[(1-i) - (1+i) \frac{\sin k_s}{1 + \cos k_s} \right] \quad (\text{E2})$$

with k_s as in Eq. (D1). Finally, for $r \neq 0$ and even L_A the result reads

$$\begin{aligned} \mathbb{F}_{m,r}(t) \approx & \frac{L_A (-1)^m}{\sqrt{8\pi t^3}} \left[i^m (2m - L_A) \cos \left(t - m\frac{\pi}{2} + \frac{\pi}{4} \right) \right. \\ & + \frac{1}{2} \left(2m \tan \frac{k_s}{2} - L_A \tan \frac{k_s}{2} + i \sec^2 \frac{k_s}{2} \right) e^{it - i\frac{\pi}{4}} - \\ & \left. (-1)^m \frac{1}{4} \text{cosec}^2 \frac{k_s}{2} \left(2i + (L_A - 2m) \sin k_s \right) e^{-it + i\frac{\pi}{4}} \right]. \end{aligned} \quad (\text{E3})$$

Notice that Eq. (E3) gives $\mathbb{F}_{m,r}(t) \sim t^{-3/2}$, which is subleading compared to Eqs. (E1) and (E2).

The corresponding asymptotic expansion for $\mathbb{G}_{m,n}(t)$ is straightforward, substituting Eqs. (E1)-(E3) into Eq. (C5). We start discussing the case with L_A odd. The result reads

$$\begin{aligned} \mathbb{G}_{m,n}(t) = & \delta_{m,n} - \frac{(-1)^{m+n}}{\pi L_A t} \sum_{r=-k_F}^{k_F} \frac{1}{1 + \cos \frac{2\pi r}{L_A}} \\ & + i \frac{e^{-2it} [(-1)^m e^{2it} + i L_A] [i(-1)^n + e^{2it} L_A]}{2\pi L_A t}. \end{aligned} \quad (\text{E4})$$

It is convenient to rewrite Eq. (E4) as

$$\mathbb{G}_{m,n}(t) = \delta_{m,n} + \frac{1}{t} u_m u_n [A(-1)^{m+n} + B(-1)^m e^{2it} + C(-1)^n e^{-2it} + D], \quad (\text{E5})$$

introducing the constants A, B, C, D as

$$A \equiv -\frac{1}{\pi L_A} \sum_{r=-k_F}^{k_F} \frac{1}{1 + \cos \frac{2\pi r}{L_A}} - \frac{1}{2\pi L_A} \quad (\text{E6})$$

$$B = C^* \equiv \frac{i}{2\pi} \quad (\text{E7})$$

$$D = -\frac{L_A}{2\pi}. \quad (\text{E8})$$

In Eq. (E5) we defined u_m as the vector of length L_A with unit entries, i.e., $u_m \equiv (1, 1, \dots, 1)$. The eigenvalues of $\mathbb{G}_{m,n}(t)$ can be calculated analytically. It turns out that \mathbb{G} has $L_A - 2$ unit eigenvalues. Only two eigenvalues contribute non trivially to the entanglement entropy, which are given as

$$\zeta_{\pm} = 1 + \frac{AL_A + DL_A \pm L_A \sqrt{A^2 + 4BC - 2AD + D^2}}{t}. \quad (\text{E9})$$

Using Eq. (B9) and Eq. (E9), and considering the limit $1 \ll L_A \ll t$, one obtains that the entropy is a scaling function of

t/L_A^2 , and can be given as

$$S_A(t) \approx \frac{L_A^2}{2\pi t} \left[1 - \log \frac{L_A^2}{2\pi t} \right]. \quad (\text{E10})$$

Clearly, since $S_A(t) > 0 \forall t$, Eq. (E10) is valid only at $t \gg L_A^2$.

We now turn to the case of L_A even. The correlation matrix $\mathbb{G}_{m,n}(t)$, keeping only terms $\mathcal{O}(t^{-1})$ is given as

$$\mathbb{G}_{m,n}(t) = \delta_{m,n} + \frac{u_m u_n}{2\pi L_A t} \times [i(-1)^m - e^{-2it} L_A][i(-1)^n e^{-2it} + L_A]. \quad (\text{E11})$$

A similar analysis as for odd L_A gives the entanglement entropy as

$$S_A(t) = - \left[1 - \frac{1 + L_A^2}{2\pi t} \right] \log \left[1 - \frac{1 + L_A^2}{2\pi t} \right] - \frac{1 + L_A^2}{2\pi t} \log \frac{1 + L_A^2}{2\pi t}. \quad (\text{E12})$$

Notice that, as expected, in the limit $1 \ll L_A$ Eq. (E12) reduces to Eq. (E10).

-
- [1] A. Polkovnikov, K. Sengupta, A. Silva, and M. Vengalattore, Rev. Mod. Phys. **83**, 863 (2011).
 - [2] I. Bloch, J. Dalibard, and W. Zwerger, Rev. Mod. Phys. **80**, 885 (2008).
 - [3] M. Rigol, V. Dunjko, and M. Olshanii, Nature **452**, 854 (2008).
 - [4] M. Greiner, O. Mandel, T. W. Hänsch, and I. Bloch, Nature **419**, 51 (2002).
 - [5] S. Hofferberth, I. Lesanovsky, B. Fischer, T. Schumm, and J. Schmiedmayer, Nature **449**, 324 (2007).
 - [6] S. Trotzky, Y.-A. Chen, A. Flesch, I. P. McCulloch, U. Schollwöck, J. Eisert, and I. Bloch, Nature Phys. **8**, 325 (2012).
 - [7] M. Cheneau, P. Barmettler, D. Poletti, M. Endres, P. Schauss, T. Fukuhara, C. Gross, I. Bloch, C. Kollath, and S. Kuhr, Nature **481**, 484 (2012).
 - [8] M. Gring, M. Kuhnert, T. Langen, T. Kitagawa, B. Rauer, M. Schreitl, I. Mazets, D. A. Smith, E. Demler, and J. Schmiedmayer, Science **337**, 1318 (2012).
 - [9] F. Meinert, M. J. Mark, E. Kirilov, K. Lauber, P. Weinmann, A. J. Daley, and H.-C. Nägerl, Phys. Rev. Lett. **111**, 053003 (2013).
 - [10] T. Kinoshita, T. Wenger, and D. S. Weiss, Nature **440**, 900 (2006).
 - [11] U. Schneider, L. Hackermüller, J. P. Ronzheimer, S. Will, S. Braun, T. Best, I. Bloch, E. Demler, S. Mandt, D. Rasch, and A. Rosch, Nature Phys. **8**, 213 (2012).
 - [12] J. P. Ronzheimer, M. Schreiber, S. Braun, S. S. Hodgman, S. Langer, I. P. McCulloch, F. Heidrich-Meisner, I. Bloch, and U. Schneider, Phys. Rev. Lett. **110**, 205301 (2013).
 - [13] A. Reinhard, J.-F. Riou, L. Zundel, D. S. Weiss, S. Li, A. M. Rey, and R. Hipolito, Phys. Rev. Lett. **110**, 033001 (2013).
 - [14] C. Holzhey, F. Larsen, and F. Wilczek, Nucl. Phys. B **424**, 443 (1994).
 - [15] G. Vidal, J. I. Latorre, E. Rico, and A. Kitaev, Phys. Rev. Lett. **90**, 227902 (2003).
 - [16] J. I. Latorre, E. Rico, and G. Vidal, Quant. Inf. Comp. **4**, 048 (2004).
 - [17] P. Calabrese and J. Cardy, J. Stat. Mech. (2004) P06002.
 - [18] L. Amico, R. Fazio, A. Osterloh, and V. Vedral, Rev. Mod. Phys. **80**, 517 (2008).
 - [19] P. Calabrese, J. Cardy, and B. Doyon, J. Phys. A **42**, 500301 (2009).
 - [20] J. Eisert, M. Cramer, and M. B. Plenio, Rev. Mod. Phys. **82**, 277 (2010).
 - [21] P. Calabrese and J. Cardy, J. Stat. Mech. (2007) P10004,
 - [22] P. Calabrese and J. Cardy, J. Stat. Mech. (2007) P06008.
 - [23] J.-M. Stéphan and J. Dubail, J. Stat. Mech. (2011) P08019.
 - [24] V. Eisler and I. Peschel, J. Stat. Mech. (2007) P06005.
 - [25] V. Eisler, F. Iglói, and I. Peschel, J. Stat. Mech. (2009) P02011.
 - [26] M. Fagotti and P. Calabrese, Phys. Rev. A **78**, 010306 (2008).
 - [27] F. Iglói, Z. Szatmari, and Y.-C. Lin, Phys. Rev. B **80**, 024405 (2009).
 - [28] B. Hsu, E. Grosfeld, and E. Fradkin, Phys. Rev. B **80**, 235412 (2009).
 - [29] U. Divakaran, F. Iglói, and H. Rieger, J. Stat. Mech. (2011) P10027.
 - [30] F. Iglói, Z. Szatmari, and Y.-C. Lin, Phys. Rev. B **85**, 094417 (2012).

- [31] K. Schönhammer, Phys. Rev. B **75**, 205329 (2007).
- [32] G. C. Levine, M. J. Bantegui, and J. A. Burg, Phys. Rev. B **86**, 174202 (2012).
- [33] T. Sabetta and G. Misguich, Phys. Rev. B **88**, 245114 (2013).
- [34] V. Eisler and Z. Rácz, Phys. Rev. Lett. **110**, 060602 (2013).
- [35] M. Collura, S. Sotiriadis, and P. Calabrese, J. Stat. Mech. (2013) P09025.
- [36] L. Bucciattini, M. Kormos, and P. Calabrese, J. Phys. A: Math. Theor. **47**, 175002 (2014).
- [37] G. De Chiara, S. Montangero, P. Calabrese, and R. Fazio, J. Stat. Mech. (2006) P03001.
- [38] A. Läuchli and C. Kollath, J. Stat. Mech. (2008) P05018.
- [39] V. Eisler and I. Peschel, EPL **99**, 20001 (2012).
- [40] H. Kim and D. A. Huse, Phys. Rev. Lett. **111**, 127205 (2013).
- [41] M. Collura and P. Calabrese, J. Phys. A: Math. Theor. **46**, 175001 (2013).
- [42] P. Hauke and L. Tagliacozzo, Phys. Rev. Lett. **111**, 207202 (2013).
- [43] J. Schachenmayer, B. P. Lanyon, C. F. Roos, and A. J. Daley, Phys. Rev. X **3**, 031015 (2013).
- [44] S. Kessler, I. P. McCulloch, and F. Marquardt, New J. Phys. **15**, 053043 (2013).
- [45] M. Collura, M. Kormos, and P. Calabrese, J. Stat. Mech. (2014) P01009.
- [46] A. Zamora, J. Rodriguez-Laguna, M. Lewenstein, and L. Tagliacozzo, arXiv:1401.7916.
- [47] P. Calabrese and J. Cardy, J. Stat. Mech. (2005) P04010.
- [48] A. J. Daley, H. Pichler, J. Schachenmayer, and P. Zoller, Phys. Rev. Lett. **109**, 020505 (2012).
- [49] D. A. Abanin and E. Demler, Phys. Rev. Lett. **109**, 020504 (2012).
- [50] J. Mossel, G. Palacios, and J.-S. Caux, J. Stat. Mech. L09001 (2010).
- [51] T. Kinoshita, T. Wenger, and D. S. Weiss, Science **305**, 1125 (2004).
- [52] M. Rigol and A. Muramatsu, Phys. Rev. Lett. **94**, 240403 (2005).
- [53] M. Rigol and A. Muramatsu, Phys. Rev. Lett. **93**, 230404 (2004).
- [54] M. Rigol and A. Muramatsu, Mod. Phys. Lett. B **19**, 861 (2005).
- [55] A. Minguzzi and D. M. Gangardt, Phys. Rev. Lett. **94**, 240404 (2005).
- [56] D. M. Gangardt and M. Pustilnik, Phys. Rev. A **77**, 041604 (2008).
- [57] F. Heidrich-Meisner, M. Rigol, A. Muramatsu, A. E. Feiguin, and E. Dagotto, Phys. Rev. A **78**, 013620 (2008).
- [58] F. Heidrich-Meisner, S. R. Manmana, M. Rigol, A. Muramatsu, A. E. Feiguin, and E. Dagotto, Phys. Rev. A **80**, 041603(R) (2009).
- [59] S. Langer, M. J. A. Schuetz, I. P. McCulloch, U. Schollwöck, and F. Heidrich-Meisner, Phys. Rev. A **85**, 043618 (2012).
- [60] L. Vidmar, S. Langer, I. P. McCulloch, U. Schneider, U. Schollwöck, and F. Heidrich-Meisner, Phys. Rev. B **88**, 235117 (2013).
- [61] J. Kajala, F. Massel, and P. Törmä, Phys. Rev. Lett. **106**, 206401 (2011).
- [62] T. Antal, Z. Rácz, A. Rákos, and G. M. Schütz, Phys. Rev. E **59**, 4912 (1999).
- [63] D. Karevski, Eur. J. Phys. B **27**, 147 (2002).
- [64] D. Gobert, C. Kollath, U. Schollwöck, and G. Schütz, Phys. Rev. E **71**, 036102 (2005).
- [65] R. Steinigeweg, J. Gemmer, and M. Michel, EPL **75**, 75406 (2006).
- [66] L. Santos, Phys. Rev. E **78**, 031125 (2008).
- [67] M. Haque, Phys. Rev. A **82**, 012108 (2010).
- [68] J. Lancaster and A. Mitra, Phys. Rev. E **81**, 06134 (2010).
- [69] J. Lancaster, E. Gull, and A. Mitra, Phys. Rev. B **82**, 235124 (2010).
- [70] J. Mossel and J.-S. Caux, New J. Phys. **12**, 055028 (2010).
- [71] S. Jesenko and M. Znidaric, Phys. Rev. B **84**, 174438 (2011).
- [72] L. Santos and A. Mitra, Phys. Rev. E **84**, 016206 (2011).
- [73] J. C. Halimeh, A. Wöllert, I. P. McCulloch, U. Schollwöck, and T. Barthel, Phys. Rev. A **89**, 063603 (2014).
- [74] X. Zotos, F. Naef, and P. Prelovšek, Phys. Rev. B **55**, 11029 (1997).
- [75] F. Heidrich-Meisner, A. Honecker, and W. Brenig, Eur. Phys. J. Spec. Topics **151**, 135 (2007).
- [76] S. R. White, Phys. Rev. Lett. **69**, 2863 (1992).
- [77] U. Schollwöck, Rev. Mod. Phys. **77**, 259 (2005).
- [78] U. Schollwöck, Annals of Physics **326**, 96 (2011).
- [79] S. Langer, F. Heidrich-Meisner, J. Gemmer, I. P. McCulloch, and U. Schollwöck, Phys. Rev. B **79**, 214409 (2009).
- [80] S. Langer, M. Heyl, I. P. McCulloch, and F. Heidrich-Meisner, Phys. Rev. B **84**, 205115 (2011).
- [81] R. Steinigeweg, S. Langer, F. Heidrich-Meisner, I. P. McCulloch, and W. Brenig, Phys. Rev. Lett. **106**, 160602 (2011).
- [82] M. Ganahl, E. Rabel, F. H. L. Essler, and H. G. Evertz, Phys. Rev. Lett. **108**, 077206 (2012).
- [83] T. Fukuhara, P. Schausz, M. Endres, S. Hild, M. Cheneau, I. Bloch, and C. Gross, Nature **502**, 76 (2013).
- [84] T. Fukuhara, A. Kantian, M. Endres, M. Cheneau, P. Schausz, S. Hild, D. Bellem, U. Schollwöck, T. Giamarchi, C. Gross, I. Bloch, S. Kuhr, Nature **9**, 235 (2013).
- [85] V. Zauner, M. Ganahl, H. G. Evertz, and T. Nishino, arXiv:1207.0862.
- [86] C. Karrasch, J. E. Moore, and F. Heidrich-Meisner, Phys. Rev. B **89**, 075139 (2014).
- [87] F. Iglói, G. Roós, and L. Turban, J. Stat. Mech. (2014) P03023.
- [88] T. Antal, Z. Rácz, and L. Sasvári, Phys. Rev. Lett. **78**, 167 (1997).
- [89] M. Rigol, V. Dunjko, V. Yurovsky, and M. Olshanii, Phys. Rev. Lett. **98**, 50405 (2007).
- [90] P. Calabrese, M. Mintchev, and E. Vicari, Phys. Rev. Lett. **107**, 020601 (2011).
- [91] P. Calabrese, M. Mintchev, and E. Vicari, J. Stat. Mech. (2011) P09028.
- [92] E. Vicari, Phys. Rev. A **85**, 062324 (2012).
- [93] A. J. Daley, C. Kollath, U. Schollwöck, and G. Vidal, J. Stat. Mech. (2004) P04005.
- [94] S. White and A. Feiguin, Phys. Rev. Lett. **93**, 266402 (2004).
- [95] H.-J. Mikeska and A. K. Kolezhuk, Lecture Notes in Physics **645**, 1 (2004).
- [96] H. W. J. Blöthe, J. Cardy, and M. P. Nightingale, Phys. Rev. Lett. **56**, 742 (1986).
- [97] I. Affleck, Phys. Rev. Lett. **56**, 746 (1986).
- [98] P. di Francesco, P. Mathieu, and D. Senechal, *Conformal field theory*, Springer (1997).
- [99] P. Ginsparg, *Fields, Strings and Critical Phenomena*, Les Houches, Session XLIX, 1988 ed. by E. Brézin and J. Zinn-Justin, (1989).
- [100] V. Eisler, D. Karevski, T. Platini, and I. Peschel, J. Stat. Mech. (2008) P01023.
- [101] I. Peschel and V. Eisler, J. Phys. A: Math. Theor. **42**, 504003 (2009).
- [102] T. Antal, P. L. Krapivsky, and A. Rákos, Phys. Rev. E **78**, 061115 (2008).
- [103] F. Iglói, G. Roós, and Y.-C. Lin, New J. Phys. **15**, 023036 (2013).

- (2013).
- [104] P. Calabrese and J. Cardy, Phys. Rev. Lett. **96**, 136801 (2006).
 - [105] V. Eisler and I. Peschel, J. Stat. Mech. (2014) P04005.
 - [106] I. Peschel, M. Kaulke, and O. Legeza, Ann. Physik (Lipzig) **8**, 153 (1999).
 - [107] I. Peschel and M.-C. Chung, J. Phys. A **32**, 8419 (1999).
 - [108] M.-C. Chung and I. Peschel, Phys. Rev. B **64**, 064412 (2001).
 - [109] I. Peschel, J. Phys. A **36**, L205 (2003).
 - [110] I. Peschel, J. Stat. Mech. (2004) P06004.
 - [111] S. Langer, Diploma thesis, RWTH Aachen 2009.
 - [112] J. Des Cloizeaux and M. Gaudin, J. Math. Phys. **7**, 1384 (1966).
 - [113] E. Lieb, T. Schultz, and D. Mattis, Ann. Phys. **16**, 407 (1961).
 - [114] E. Barouch, B. M. McCoy, and M. Dresden, Phys. Rev. A **2**, 1075 (1970).
 - [115] E. Barouch and B. McCoy, Phys. Rev. A **3**, 786 (1971).
 - [116] E. Barouch and B. M. McCoy, Phys. Rev. A **3**, 2137 (1971).
 - [117] B. M. McCoy, E. Barouch, and D. B. Abraham, Phys. Rev. A **4**, 2331 (1971).
 - [118] J. I. Latorre and A. Riera, J. Phys. A **42**, 504002 (2009).
 - [119] M. Fagotti and P. Calabrese, J. Stat. Mech. (2010) P04016.
 - [120] V. Alba, L. Tagliacozzo, and P. Calabrese, Phys. Rev. B **81**, 060411(R) (2010).
 - [121] V. Alba, L. Tagliacozzo, and P. Calabrese, J. Stat. Mech. (2011) P06012.
 - [122] F. Iglói and I. Peschel, Europhys. Lett. **89**, 40001 (2010).
 - [123] M. Fagotti and P. Calabrese, J. Stat. Mech. (2011) P01017.
 - [124] M. Fagotti, EPL **97**, 17007 (2012).
 - [125] J. H. H. Perk and H. W. Capel, Physica A **89**, 265 (1977).
 - [126] J. H. H. Perk and H. Au-Yang, J. Stat. Phys. **135**, 599 (2009).
 - [127] E. H. Lieb and D. W. Robinson, Commun. Math. Phys. **28**, 251 (1972).
 - [128] A. Erdélyi, *Asymptotic Expansions*, New York: Dover Publications (1956).